

1 **Oligomer formation from the gas-phase reactions of Criegee**
2 **intermediates with hydroperoxide esters: mechanism and kinetics**

3 Long Chen,^{1,2} Yu Huang,^{*,1,2} Yonggang Xue,^{1,2} Zhihui Jia,³ Wenliang Wang⁴

4 ¹ *State Key Lab of Loess and Quaternary Geology (SKLLQG), Institute of Earth*
5 *Environment, Chinese Academy of Sciences (CAS), Xi'an, 710061, China*

6 ² *CAS Center for Excellence in Quaternary Science and Global Change, Xi'an,*
7 *710061, China*

8 ³ *School of Materials Science and Engineering, Shaanxi Normal University, Xi'an,*
9 *Shaanxi, 710119, China*

10 ⁴ *School of Chemistry and Chemical Engineering, Key Laboratory for*
11 *Macromolecular Science of Shaanxi Province, Shaanxi Normal University, Xi'an,*
12 *Shaanxi, 710119, China*

13

14

15

16 Submitted to *Atmospheric Chemistry & Physics*

17

18

19 *Corresponding author:

20 Prof. Yu Huang, E-mail address: huangyu@ieecas.cn

21

22 Abstract

23 Hydroperoxide esters, formed in the reactions of carbonyl oxides (also called
24 Criegee intermediates, CIs) with formic acid, play a crucial role in the formation of
25 secondary organic aerosol (SOA) in the atmosphere. However, the transformation
26 mechanism of hydroperoxide esters in the presence of stabilized Criegee
27 intermediates (SCIs) is not well understood. Herein, the oligomerization reaction
28 mechanisms and kinetics of distinct SCIs (CH_2OO , *syn*- CH_3CHOO , *anti*- CH_3CHOO
29 and $(\text{CH}_3)_2\text{COO}$) reactions with their respective hydroperoxide esters as well as with
30 hydroperoxymethyl formate (HPMF) are investigated in the gas phase using quantum
31 chemical and kinetics modeling methods. The calculations show that the addition
32 reactions of SCIs with hydroperoxide esters proceed through successive insertion of
33 SCIs into hydroperoxide ester to form oligomers that involve SCIs as the repeated
34 chain unit. The saturated vapour pressure and saturated concentration of the formed
35 oligomers decrease monotonically as the number of SCIs is increased. The
36 exothermicity of oligomerization reactions decreases significantly when the number
37 of methyl substituents increases, and the exothermicity of *anti*-methyl substituted
38 carbonyl oxides is obviously higher than that of *syn*-methyl substituted carbonyl
39 oxides. The $-\text{OOH}$ insertion reaction is energetically more feasible than the $-\text{CH}$
40 insertion pathway in the SCIs oligomerization reactions, and the barrier heights
41 increase with increasing the number of SCIs added to the oligomer except
42 *syn*- CH_3CHOO . For the reactions of distinct SCIs with HPMF, the barrier of $-\text{OOH}$
43 insertion pathway shows a dramatic decrease when a methyl substituent occurs at the
44 *anti*-position, while it reveals a significant increase when a methyl group is introduced
45 at the *syn*-position and dimethyl substituent. Compared with the rate coefficients of
46 the $\text{CH}_2\text{OO} + \text{HPMF}$ reaction, the rate coefficients increase by about one order of
47 magnitude when a methyl substituent occurs at the *anti*-position, whereas the rate
48 coefficients decrease by 1-2 orders of magnitude when a methyl group is introduced
49 at the *syn*-position. These new findings advance our current understanding on the
50 influence of Criegee-chemistry on the formation and growth processes as well as the

51 chemical compositions of SOA.

52 **1. Introduction**

53 Alkenes are an important class of volatile organic compounds (VOCs) that are
54 emitted into the atmosphere from large quantities of biogenic and anthropogenic
55 sources (Lester and Klippenstein, 2018). The reaction with ozone is one of the
56 dominant degradation pathways for alkenes in the atmosphere (Johnson and Marston,
57 2008; Atkinson and Arey, 2003). Ozonolysis of alkene proceeds through the
58 electrophilic 1,3-cycloaddition of ozone to C=C bond of alkenes to form a primary
59 ozonides (POZ), and then it rapidly decomposes into a carbonyl compound and a
60 carbonyl oxide (also called Criegee intermediates, CIs) (Criegee, 1975; Osborn and
61 Taatjes, 2015; Giorio et al., 2017). A part of the initially energized CIs (~ 37-50%)
62 may promptly dissociate to OH radicals, which are thought to be an important
63 nonphotolytic source of OH radicals in the atmosphere (Novelli et al., 2014; Liu et al.,
64 2014). The remaining CIs (~ 63-50%) are collisionally stabilized prior to the thermal
65 unimolecular decay (Lester and Klippenstein, 2018; Novelli et al., 2014; Anglada and
66 Solé, 2016). The stabilized Criegee intermediates (SCIs) can proceed bimolecular
67 reactions with various trace species such as H₂O, NO₂, SO₂, and HCOOH to generate
68 secondary organic aerosol (SOA), thus profoundly influencing air quality, global
69 climate and human health (Osborn and Taatjes, 2015; Khan et al., 2018; Lin and Chao,
70 2017; Liu et al., 2019; Chhantyal-Pun et al., 2018; Gong and Chen, 2021; Taatjes,
71 2017).

72 Formic acid (HCOOH), one of the most abundant carboxylic acids, has a
73 significant influence on rainwater acidity in remote areas, where pH reduces by
74 0.25-0.5 in the presence of HCOOH (Stavrakou et al., 2012; Wang et al., 2020;
75 Chaliyakunnel et al., 2016). It also plays an important role in the formation of cloud
76 condensation nuclei (CCN), indirectly influencing radiative forcing and climate
77 change (Yu, 2000). The primary sources of HCOOH include biomass burning, human
78 activities, tropical and boreal forests, as well as the secondary sources involve the
79 photochemical oxidation of non-methane hydrocarbons, such as ketene-enols, vinyl

80 alcohol, isoprene, and terpenoids (Stavrakou et al., 2012; Wang et al., 2020;
81 Chaliyakunnel et al., 2016; So et al., 2014; Paulot et al., 2011). According to satellite
82 measurements, the production of HCOOH is up to 100-120 Tg yr⁻¹, and the value is
83 expected to increase due to the acceleration of industrialization and urbanization
84 (Stavrakou et al., 2012). Recent kinetics measurements have revealed that the reaction
85 with HCOOH is a more important loss process for SCI than is presently assumed,
86 especially in terrestrial equatorial areas and in high SCI concentration areas (Welz et
87 al., 2014; Chung et al., 2019). The formed hydroperoxide esters have been identified
88 as the low-volatility and high-oxygenated compounds, contributing to the formation
89 and growth of SOA (Welz et al., 2014; Vansco et al., 2021; Sakamoto et al., 2017;
90 Riva et al., 2017).

91 Welz et al. (2014) directly determined the rate coefficients for the reactions of
92 CH₂OO and CH₃CHOO with formic and acetic acid by employing multiplexed
93 photoionization mass spectrometry and cavity-enhanced broadband ultraviolet
94 absorption spectroscopy. They found that the measured rate coefficients are in the
95 excess of $1.0 \times 10^{-10} \text{ cm}^3 \text{ molecule}^{-1} \text{ s}^{-1}$, which are several orders of magnitude greater
96 than those derived from previous experimental studies (Johnson et al., 2001; Tobias
97 and Ziemann, 2001). Sipilä et al. conducted a competitive reaction kinetics
98 experiment to investigate the reactions of acetone oxide ((CH₃)₂OO) with SO₂,
99 HCOOH and CH₃COOH, and they concluded that the rate coefficients of the
100 (CH₃)₂OO + HCOOH/CH₃OOH reactions are faster than that of the (CH₃)₂OO + SO₂
101 system by about three times (Sipilä et al., 2014). These high rate coefficients could
102 make the reaction with carboxylic acids a substantial dominant chemical sink for
103 carbonyl oxides in the atmosphere (Welz et al., 2014; Taatjes et al., 2019;
104 Chhantyal-Pun et al., 2017). Quantum chemical calculations show that the reaction of
105 CH₂OO with HCOOH proceeds through a facile transfer of hydrogen atom from the
106 acidic OH group to the terminal oxygen of CH₂OO to form hydroperoxymethyl
107 formate (HPMF) (Long et al., 2009; Vereecken, 2017; Porterfield et al., 2019). Chen
108 et al. (2018) concluded the same by investigating the reactions of various carbonyl
109 oxides with HCOOH that the barrierless 1,4-insertion reaction is the most favorable

110 pathway, and the primary products are hydroperoxide esters. Caravan et al. (2020)
111 employed high-level ab initio CCSD(T)-F12 methods to study the reaction of methyl
112 vinyl ketone oxide (MVK-oxide) with HCOOH, and they found that the barrierless
113 net insertion of MVK-oxide into HCOOH leading to the formation of a functionalized
114 hydroperoxide is dominant over fragmentation to produce an alkoxy radical and OH
115 radicals. Moreover, oligomerization reactions with hydroperoxides and peroxy
116 radicals are identified as one of the dominant loss processes for carbonyl oxides under
117 atmospheric conditions (Sakamoto et al., 2013; Sadezky et al., 2008; Zhao et al., 2015;
118 Chen et al., 2017 and 2019). All the above milestone investigations provide important
119 information for understanding the chemistry of Criegee intermediate in the presence
120 of carboxylic acids. However, to the best of our knowledge, there are few studies on
121 the oligomerization reactions of SCIs with hydroperoxide esters, which are important
122 with regard to organic new particle and cloud condensation nuclei formations.
123 Moreover, the relationship between the reactivity of SCIs and the nature of
124 substituents remains uncertain in the SCIs oligomerization reactions.

125 In the present study, we mainly focus on the oligomerization reaction
126 mechanisms and kinetics of four carbonyl oxides reactions with their respective
127 hydroperoxide esters as well as with HPMF by employing quantum chemical
128 calculations and kinetics modeling methods. For the initiation reactions of carbonyl
129 oxides with formic acid, four kinds of pathways including 1,4 O-H insertion, 1,2 O-H
130 insertion, C-H insertion, and C=O cycloaddition are considered. For the
131 oligomerization reactions of the successive insertion of carbonyl oxides into
132 hydroperoxide esters, two types of reactions involving –OOH and –CH insertions are
133 taken into account. The selected carbonyl oxides, including CH₂OO, *syn*-,
134 *anti*-CH₃CHOO and (CH₃)₂CHOO, are anticipated upon the ozonolysis of ethylene,
135 propylene, and 2,3-dimethyl-2-butene, whereas the hydroperoxide esters are assumed
136 to arise from the bimolecular reactions of carbonyl oxides with formic acid in the
137 atmosphere.

138 2. Computational details

2.1 Electronic structure and energy calculations

The geometries of all stationary points, including reactants (R), intermediates (IM), transition states (TS), and products (P), are optimized at the M06-2X/6-311+G(2df,2p) level of theory, since the M06-2X functional has the reliable performance for predicting thermochemistry, kinetics and hydrogen bonding interactions (Zhao and Truhlar, 2008). Harmonic vibrational frequencies are performed at the same level to verify the nature of transition state (NIMAG = 1) and minimum (NIMAG = 0), and to provide zero-point vibrational energy (ZPVE) and Gibbs free energies corrections (G_{corr}), which are scaled by a factor of 0.98 (Alecú et al., 2010). Intrinsic reaction coordinate (IRC) calculations are carried out to verify that each transition state is connected to the desired reactant and product (Fukui, 1981). The single point energy (SPE) calculations are performed at the M06-2X/ma-TZVP level of theory based on the M06-2X/6-311+G(2df,2p) optimized geometries. Moreover, the basis set superposition error (BSSE) is performed by using the counterpoise method proposed by Boys and Bernardi (1970) to evaluate the stability of the pre-reactive complex (RC). Herein, the Gibbs free energy (G) is defined as the sum of SPE and Gibbs correction ($G = E + G_{\text{corr}}$). Electronic energy (ΔE^\ddagger) and Gibbs free energy (ΔG^\ddagger) barriers are defined as the difference in energy between a TS and a RC ($\Delta E^\ddagger = E_{\text{TS}} - E_{\text{RC}}$ and $\Delta G^\ddagger = G_{\text{TS}} - G_{\text{RC}}$). Reaction Gibbs free energy (ΔG) is defined as the difference in energy between a P and a R ($\Delta G = G_{\text{P}} - G_{\text{R}}$).

To further assess the reliability of the selected M06-2X/ma-TZVP method for SPE calculations, the single point energies of all stationary points involved in the initiation reactions of distinct SCIs with HCOOH are recalculated at the high-accuracy CCSD(T)/6-311+G(2df,2p) and QCISD(T)/6-311+G(2df,2p) levels of theory. The calculated results are summarized in Table S1. This table shows that the ΔE^\ddagger and ΔG^\ddagger obtained using the QCISD(T) method are in excellent agreement with those obtained using the CCSD(T) approach. It is therefore that the energies obtained using the CCSD(T) method are used as the benchmark for comparison. The mean

168 absolute deviations (MAD) of ΔE^\ddagger and ΔG^\ddagger between the CCSD(T) and M06-2X
169 methods are 0.43 and 0.41 kcal mol⁻¹, respectively; the largest deviations of ΔE^\ddagger and
170 ΔG^\ddagger are 1.0 and 1.1 kcal mol⁻¹, respectively. These results reveal that the energies
171 obtained using the M06-2X method are close to those obtained using the CCSD(T)
172 approach. Therefore, the M06-2X/ma-TZVP method is suitable to investigate the
173 SCIs oligomerization reactions. In the following discussion, the energies are applied
174 in terms of Gibbs free energy to describe the reaction mechanism unless otherwise
175 stated. All electronic structure calculations are carried out by using Gaussian 09
176 program (Frisch et al., 2009). The Multiwfn program and Visual molecular dynamics
177 (VMD) are utilized to analysis and visualize the molecular orbitals of the relevant
178 species (Lu and Chen, 2012; Humphrey et al., 1996).

179 **2.2 Kinetics calculations**

180 The rate coefficients for the barrierless 1,4 O-H insertion reactions are computed
181 by employing the variable-reaction-coordinate variational transition-state theory
182 (VRC-VTST) (Bao and Truhlar, 2017), in which the potential energies are calculated
183 by direct dynamics using the M06-2X/6-311+G(2df,2p) method. Rate coefficients for
184 the SCIs + HCOOH reactions are calculated using the E, J -resolved microcanonical
185 variational theory (E, J - μ VT) using a single-faceted dividing surface. In the
186 VRC-VTST calculations, the reaction coordinate s is defined by pivot points, which
187 are used to orientate the reactants 1 and 2. s is defined as the minimal value of r_{ij} ,
188 where r_{ij} is the distance between pivot points i and j , i is a pivot point on reactant 1
189 and j is a pivot point on reactant 2. Two of the pivot points are located at a distance $\pm d$
190 from the center of mass (COM) of SCIs, and the other two pivot points are located at
191 a distance $\pm d$ from the COM of HCOOH with a fixed length of 0.05, 0.10, 0.15, 0.2
192 and 0.25 Å. Then, for a given choice of pivot points, the variationally lowest rate
193 coefficients are minimized with respect to s at each of the temperatures. We observed
194 that $d=0.05$ produces the best variation results and only its value is reported in the
195 present study.

196 The rate coefficients for the bimolecular reactions with the tight transition states

197 are calculated by using the canonical transition state theory (CTST) along with
 198 one-dimensional asymmetric Eckart tunneling correction (Truhlar et al., 1996; and
 199 Eckart, 1930). As shown in Fig. 1, the entrance pathway Entry2 of R₁R₂COO reaction
 200 with HCOOH consists of two steps: (i) an intermediate IMent2 is formed via a
 201 barrierless process; (ii) then, it rearranges to the product Pent2 through a tight
 202 transition state TSent2. The whole reaction process can be described as Eq. (1):



204 Assuming the rapid equilibrium is established between the IMent2 and reactants.
 205 According to the steady-state approximation (SSA), the total rate coefficient is
 206 approximately expressed as Eq. (2) (Zhang et al., 2012):

$$207 \quad k_{\text{tot}} = \frac{k_1}{k_{-1} + k_2} k_2 \approx \frac{k_1}{k_{-1}} k_2 = K_{\text{eq}} k_2 \quad (2)$$

208 The equilibrium constant K_{eq} is written as Eq. (3):

$$209 \quad K_{\text{eq}} = \sigma \frac{Q_{\text{IM}}(T)}{Q_{\text{R1}}(T)Q_{\text{R2}}(T)} \exp\left(\frac{G_{\text{R}} - G_{\text{IM}}}{RT}\right) \quad (3)$$

210 where σ refers to reaction symmetry number, $Q_{\text{IM}}(T)$, $Q_{\text{R1}}(T)$ and $Q_{\text{R2}}(T)$ denote
 211 the partition functions of intermediate, reactants R1 and R2, which are equal to the
 212 multiplication of translational, rotational, vibrational and electronic partition functions
 213 ($Q = Q_{\text{rot}}Q_{\text{vib}}Q_{\text{trans}}Q_{\text{elec}}$) (Mendes et al., 2014), T is the temperature in Kelvin, R is the
 214 ideal gas constant, G_{R} and G_{IM} are the total Gibbs free energies of reactant and
 215 intermediate, respectively. The rate coefficient calculations are performed with the
 216 Polyrate 2017-C and KiSThelP 2019 programs (Canneaux et al., 2013; Zheng et al.,
 217 2018).

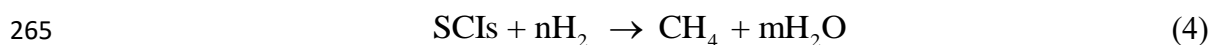
218 **3. Results and discussion**

219 **3.1 Initiation reactions of distinct SCIs with HCOOH**

220 The reaction with HCOOH is one of the dominant loss processes for SCIs and is
 221 expected to trigger the formation of SOA in the atmosphere (Chhantyal-Pun et al.,
 222 2018; Cabezas and Endo, 2020; Zhao et al., 2018; Zhou et al., 2019). The potential

223 energy surface (PES) of distinct SCIs (CH_2OO , *syn*-, *anti*- CH_3CHOO and $(\text{CH}_3)_2\text{COO}$)
224 reactions with HCOOH is drawn in Fig. 1. The geometries of all stationary points are
225 displayed in Fig. S1. The relative free energy of each stationary point and free energy
226 barrier (ΔG^\ddagger) of each elementary reaction are summarized in Table 1. As shown in Fig.
227 1, the bimolecular reaction of distinct SCIs with HCOOH proceeds via four possible
228 pathways, namely (1) 1,4 O-H insertion (Entry 1), (2) 1,2 O-H insertion (Entry 2), (3)
229 C-H insertion (Entry 3), and (4) C=O cycloaddition (Entry 4). For Entry 1, the
230 addition reaction of CH_2OO with HCOOH proceeds through the 1,4 O-H insertion of
231 CH_2OO into HCOOH to form a hydroperoxide ester $\text{HC(O)O-CH}_2\text{OO-H}$ with a
232 exoergicity of $37.6 \text{ kcal}\cdot\text{mol}^{-1}$. The formation of $\text{HC(O)O-CH}_2\text{OO-H}$ is obtained
233 through a concerted process of $\text{O}_2\text{-H}_2$ bond breaking in the HCOOH and $\text{O}_4\text{-H}_2$ and
234 $\text{C}_2\text{-O}_1$ bonds forming. Despite an attempt by various methods, the corresponding
235 transition state is still not located in the effort of optimization. To further validate the
236 barrierless process of 1,4 O-H insertion reaction, a relaxed scan over the O-H and C-O
237 bonds is performed at the M06-2X/6-311+G(2df,2p) level of theory. The scans start
238 from the optimized structure of the adduct products, and the O-H and C-O bond
239 lengths are then increased in steps of 0.10 \AA , while other geometric parameters are
240 fully optimized. The zero of energy is set to be the energy of the adduct products. The
241 electronic potential energy profiles along the O-H and C-O dissociation coordinate are
242 presented in Fig. S2. As seen in Fig. S2a, the electronic potential energy of the
243 minimum potential-energy path (MEP) decreases monotonically when the bond
244 length of the O-H and C-O bonds decreases, suggesting that the 1,4 O-H insertion
245 reaction of CH_2OO with HCOOH is indeed barrierless. Similar conclusion is also
246 obtained from the electronic potential energy profiles for the *anti*- $\text{CH}_3\text{CHOO} +$
247 HCOOH , *syn*- $\text{CH}_3\text{CHOO} + \text{HCOOH}$ and $(\text{CH}_3)_2\text{COO} + \text{HCOOH}$ (Fig. S2b-d)
248 reactions that 1,4 O-H insertion reactions are barrierless. This conclusion is further
249 supported by the analogous reaction systems that 1,4 O-H insertion reactions of
250 carbonyl oxides with carboxylic acids are a barrierless process including concerted
251 hydrogen atom transfer and new C-O bond formation (Chhantyal-Pun et al., 2017;
252 Long et al., 2009; Vereecken, 2017; Cabezas and Endo, 2019; Lin et al., 2019).

253 The exothermicities of 1,4 O-H insertion reactions of distinct SCIs with HCOOH
 254 are assessed by the reaction enthalpies ($\Delta_r H_{298}^\circ$), which are defined as the difference
 255 between the enthalpies of formation ($\Delta_f H_{298}^\circ$) of the products and reactants
 256 ($\Delta_r H_{298}^\circ = \sum_{\text{products}} \Delta_f H_{298}^\circ - \sum_{\text{reactants}} \Delta_f H_{298}^\circ$). To the best of our knowledge, there are no literature
 257 values available on the enthalpies of formation of carbonyl oxides and hydroperoxide
 258 esters except the simplest carbonyl oxide CH₂OO. Therefore, the isodesmic reaction
 259 method is adopted to obtain the enthalpies of formation, and the results are listed in
 260 Table S2. An isodesmic reaction is a hypothetical reaction, in which the type of
 261 chemical bonds in the reactants is the similar as that of chemical bonds in the products.
 262 The following isodesmic reaction is constructed because the experimental values of
 263 H₂, CH₄ and H₂O are available ($\Delta_f H_{298}^\circ(\text{H}_2) = 0.00 \text{ kcal}\cdot\text{mol}^{-1}$; $\Delta_f H_{298}^\circ(\text{CH}_4) = -17.82$
 264 $\text{kcal}\cdot\text{mol}^{-1}$; $\Delta_f H_{298}^\circ(\text{H}_2\text{O}) = -57.79 \text{ kcal}\cdot\text{mol}^{-1}$).



266 As seen in Table S2, the enthalpy of formation of CH₂OO is calculated to be
 267 23.23 kcal·mol⁻¹, which is in good agreement with the available literature values
 268 (Chen et al., 2016; Karton et al., 2013). This result implies that the theoretical method
 269 employed herein is reasonable to predict the thermochemical parameters. The
 270 enthalpies of formation of carbonyl oxides and hydroperoxide esters significantly
 271 decrease with increasing the number of methyl groups. Notably, the decreased values
 272 in the enthalpies of formation of carbonyl oxides are greater than those of
 273 hydroperoxide esters under the condition of the same number of methyl groups. For
 274 example, the enthalpy of formation of *anti*-CH₃CHOO decreases by 12.95 kcal·mol⁻¹
 275 compared to the enthalpy of formation of CH₂OO (23.23 kcal·mol⁻¹), and the enthalpy
 276 of formation of Pent1b decreases by 12.12 kcal·mol⁻¹ compared to the enthalpy of
 277 formation of Pent1a (-112.08 kcal·mol⁻¹). The reaction enthalpies of the reactions of
 278 distinct SCIs with HCOOH decrease in the order of -44.69 (CH₂OO + HCOOH →
 279 Pent1a) < -43.86 (*anti*-CH₃CHOO + HCOOH → Pent1b) < -38.13 (*syn*-CH₃CHOO +
 280 HCOOH → Pent1c) < -37.12 kcal·mol⁻¹ ((CH₃)₂COO + HCOOH → Pent1d),

281 indicating that the reaction enthalpies are highly dependent on the number and
282 location of methyl groups. The trend in reaction enthalpies is consistent with the trend
283 in the enthalpies of formation of carbonyl oxides.

284 For Entry 2, each addition reaction starts with the formation of a pre-reactive
285 hydrogen bonded complex IMent2 in the entrance channel. Then it immediately
286 converts into product Pent2 through the 1,2 O-H insertion transition state. The
287 formation of Pent2 is obtained via a concerted process of O₂-H₂ bond rupture in the
288 HCOOH and O₄-H₂ and C₂-O₂ bonds forming. The reaction barrier ΔG^\ddagger increases in
289 the order of 10.0 (CH₂OO) < 13.0 (*anti*-CH₃CHOO) < 14.6 (*syn*-CH₃CHOO) \approx 14.4
290 ((CH₃)₂COO) kcal·mol⁻¹, suggesting that the parent CH₂OO + HCOOH reaction is
291 favored kinetically. Compared with the barrier of the parent system, the barrier
292 increases by 3.0 kcal·mol⁻¹ when a methyl substitution occurs at the R₁ position, and
293 the barrier increases by \sim 5 kcal·mol⁻¹ when a methyl group is introduced at the R₂
294 position and dimethyl substituent. The aforementioned result implies that the
295 methyl-substituted CH₂OO hinders the 1,2 O-H insertion of carbonyl oxides into
296 formic acid. Notably, the exothermicity decreases significantly as the number of
297 methyl group is increased. The products Pent1 and Pent2 formed from Entry 1 and 2
298 are two conformations that differ in the orientation of the -C(O)H moiety over the -
299 OOH group. The calculated result shows that Pent1 is more stable than Pent2 in
300 energy due to the existence of intramolecular hydrogen bond between hydrogen atom
301 of -OOH group and carbonyl oxygen atom.

302 For Entry 3, the addition reaction begins with the formation of a pre-reactive
303 complex IMent3 in the entrance channel, and then it surmounts a barrier to reaction.
304 However, the barriers of C-H insertion reactions are significantly high (21.8-27.6
305 kcal·mol⁻¹), such that they are of less importance in the atmosphere. The high reaction
306 barriers might be attributed to the large bond dissociation energy (BDE) of C-H bond
307 in the formic acid. For Entry 4, the addition reaction proceeds through a cyclization
308 process of C₂-O₁ and O₄-C₁ bond forming to produce a five-membered ring compound
309 Pent4. The barrier of C=O cycloaddition reaction in the CH₂OO + HCOOH reaction is
310 5.8 kcal·mol⁻¹, which is lower than that of the corresponding channels in Entry 2 and

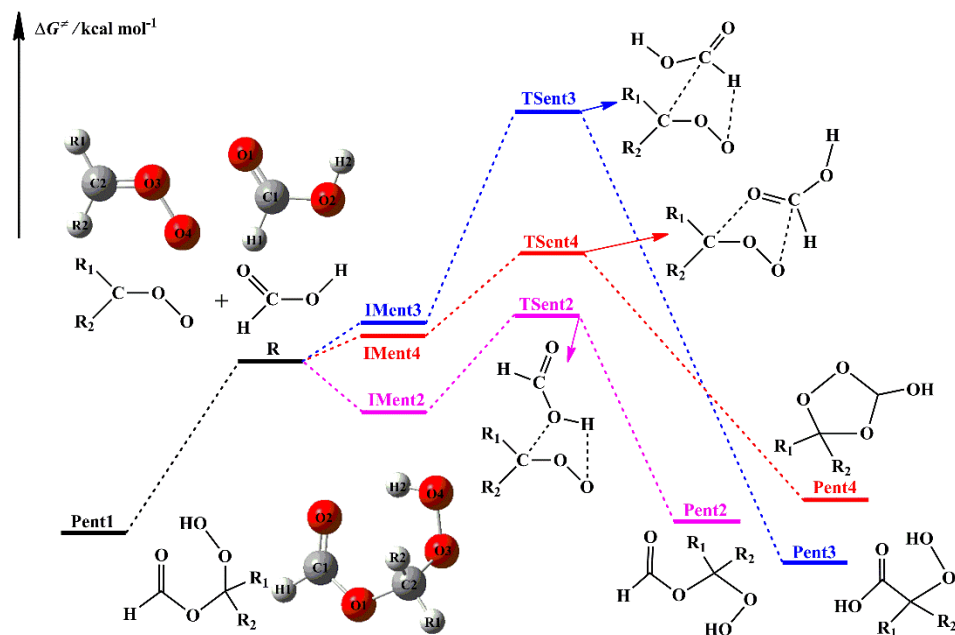
311 Entry 3 by 4.2 and 16.0 kcal·mol⁻¹, respectively. The result reveals that the C=O
312 cycloaddition reaction is feasible kinetically. A similar conclusion is also obtained
313 from the reactions of HCOOH with *syn*-, *anti*-CH₃CHOO and (CH₃)₂COO that the
314 C=O cycloaddition reactions are favored over 1,2 O-H and C-H insertion reactions.

315 The rate coefficients of each elementary pathway included in the initiation
316 reactions of distinct SCIs with HCOOH are tabulated in Table S3-S6. The total rate
317 coefficient is equal to the sum of the rate coefficient of each elementary pathway. As
318 shown in Table S3, the total rate coefficients $k_{\text{tot-CH}_2\text{OO}}$ of CH₂OO reaction with
319 HCOOH are in excess of 1.0×10^{-10} cm³ molecule⁻¹ s⁻¹, and they exhibit a slightly
320 negative temperature dependence in the temperature range of 273-400 K. At room
321 temperature, $k_{\text{tot-CH}_2\text{OO}}$ is estimated to be 1.29×10^{-10} cm³ molecule⁻¹ s⁻¹, which is in
322 good agreement with the experimental values reported by Welz et al. (2014) ($[1.1 \pm$
323 $0.1] \times 10^{-10}$), Chung et al. (2019) ($[1.4 \pm 0.3] \times 10^{-10}$), and Peltola et al. (2020) ($[1.0 \pm$
324 $0.03] \times 10^{-10}$). $k(\text{TS}_{\text{ent1}})$ is approximately equal to $k_{\text{tot-CH}_2\text{OO}}$ in the whole temperature
325 range, and it decreases in the range of 1.34×10^{-10} (273 K) to 1.05×10^{-10} (400 K)
326 cm³ molecule⁻¹ s⁻¹ with increasing temperature. $k(\text{TS}_{\text{ent1}})$ is several orders of
327 magnitude greater than $k(\text{TS}_{\text{ent2}})$, $k(\text{TS}_{\text{ent3}})$ and $k(\text{TS}_{\text{ent4}})$ over the temperature range
328 from 273 to 400 K. The result again shows that the barrierless 1,4 O-H insertion
329 reaction is predominant. It should be noted that although the barrier of Entry 2 is 4.2
330 kcal·mol⁻¹ higher than that of Entry 4, $k(\text{TS}_{\text{ent2}})$ is merely about 1-2 fold smaller than
331 $k(\text{TS}_{\text{ent4}})$. The reason is ascribed to the fact that the C=O cycloaddition reaction is
332 entropically unfavorable (Vereecken, 2017).

333 Equivalent to the case of the reaction of CH₂OO with HCOOH, the total rate
334 coefficient $k_{\text{tot-anti}}$ of *anti*-CH₃CHOO reaction with HCOOH also decreases slightly
335 with the temperature increasing (Table S4). This table shows that Entry 1 is
336 kinetically favored over Entry 2, 3 and 4, and Entry 2 is competitive with Entry 4 in
337 the temperature range of 273-400 K. Similar conclusion is also obtained from the
338 results of the rate coefficients for the reactions of *syn*-CH₃CHOO and (CH₃)₂COO
339 with HCOOH that Entry 1 is the dominant pathway (Table S5-S6). It deserves
340 mentioning that the competition of Entry 2 is significantly greater than that of Entry 4

341 in the *syn*-CH₃CHOO + HCOOH and (CH₃)₂COO + HCOOH systems. Based on the
342 above discussions, it can be concluded that the relative importance of different
343 pathways is highly dependent on the number and location of methyl substituents in
344 the carbonyl oxides. Notably, the rate coefficient of each elementary pathway
345 included in the *anti*-CH₃CHOO + HCOOH reaction is several orders of magnitude
346 greater than that of the corresponding channel involved in the other SCIs + HCOOH
347 systems. It is because that *anti*-CH₃CHOO is substantially more reactive toward
348 HCOOH than other SCIs. Similar phenomenon has also observed from the reactivity
349 of *anti*-CH₃CHOO toward water and SO₂ (Taatjes et al., 2013; Long et al., 2016;
350 Huang et al., 2015; Cabezas and Endo, 2018). At ambient temperature, the total rate
351 coefficients of HCOOH reactions with *anti*-CH₃CHOO, *syn*-CH₃CHOO and
352 (CH₃)₂COO are estimated to be 5.22, 2.18 and 3.97×10^{-10} cm³ molecule⁻¹ s⁻¹,
353 respectively, which are consistent with the prior experimental measurements of 5 ± 3 ,
354 2.5 ± 0.3 and $4.5 \pm 0.9 \times 10^{-10}$ cm³ molecule⁻¹ s⁻¹ (Welz et al., 2014; Sipilä et al.,
355 2014).

356 In summary, the barrierless 1,4 O-H insertion reaction is the dominant pathway
357 in the initiation reactions of distinct SCIs with HCOOH. This conclusion is consistent
358 with the recent experimental results derived from the reactions of formic acid with
359 methacrolein oxide (MACR-OO) and methyl vinyl ketone oxide (MVK-OO) that the
360 1,4-addition mechanism is energetically favorable (Vansco et al., 2021; Caravan et al.,
361 2020). Therefore, in the present study, the adduct products Pent1 formed from the
362 barrierless 1,4 O-H insertion of carbonyl oxides into HCOOH are selected as the
363 model compounds to investigate the oligomerization reaction mechanisms of carbonyl
364 oxides reactions with hydroperoxide esters.



365

366 **Figure 1.** Schematic PES for the possible entrance pathways of the initiation reactions of HCOOH
 367 with various SCIs (black, pink, blue, and red lines represent 1,4 O-H insertion, 1,2 O-H insertion,
 368 C-H insertion, and C=O cycloaddition reactions, respectively)

369 **Table 1** Relative free energies of stationary points and free-energy barriers (ΔG^\ddagger) at 298 K in kcal
 370 mol⁻¹ for the various SCIs (R₁R₂COO, R₁, R₂=H, CH₃) reactions with HCOOH calculated at the
 371 M06-2X/ma-TZVP//M06-2X/6-311+G(2df,2p) level of theory

Entry	R1	R2	IMent	TSent	Pent	ΔG^\ddagger
1	H	H	–	–	-37.6	–
	CH ₃	H	–	–	-34.0	–
	H	CH ₃	–	–	-29.8	–
	CH ₃	CH ₃	–	–	-25.6	–
2	H	H	-3.1	6.9	-37.3	10.0
	CH ₃	H	-11.0	2.0	-33.7	13.0
	H	CH ₃	-6.6	8.0	-29.1	14.6
	CH ₃	CH ₃	-8.8	5.6	-24.9	14.4
3	H	H	3.4	25.2	-46.9	21.8
	CH ₃	H	1.8	24.0	-41.5	22.2
	H	CH ₃	3.0	30.6	-37.6	27.6
	CH ₃	CH ₃	1.9	29.5	-33.0	27.6
4	H	H	3.4	9.2	-31.7	5.8
	CH ₃	H	2.2	7.8	-29.4	5.6
	H	CH ₃	3.5	14.6	-25.3	11.1
	CH ₃	CH ₃	3.0	13.2	-22.9	10.2

372 **3.2. The reactions of distinct SCIs with their respective**

373 **hydroperoxide esters**

374 The formed hydroperoxide ester has two possible unimolecular decay pathways.
375 The first is the direct O-O bond rupture resulting in the formation of
376 oxylmethylformate and OH radicals (Vereecken, 2017). The second is the –OH
377 fragment binding to adjacent hydrogen atom leading to the formation of anhydride
378 and H₂O (Aplincourt and Ruiz-López, 2000; Neeb et al., 1998). However, the barriers
379 of these two unimolecular reactions are extremely high, such that they are of less
380 importance in the atmosphere. The formed hydroperoxide ester possess –OOH and –
381 OC(O)H groups, both of them can serve as the reactive moieties to react with
382 carbonyl oxides giving rise to the formation of oligomers. In the present study, we
383 mainly consider two types of pathways: (a) –OOH insertion and (b) –CH insertion,
384 while the C=O cycloaddition reaction is not taken into account because it is
385 entropically unfavorable (Vereecken, et al., 2017; Lin et al., 2009). The
386 aforementioned reactions are discussed in detail in the following subsections.

387 **3.2.1 The reactions of 2CH₂OO with Pent1a**

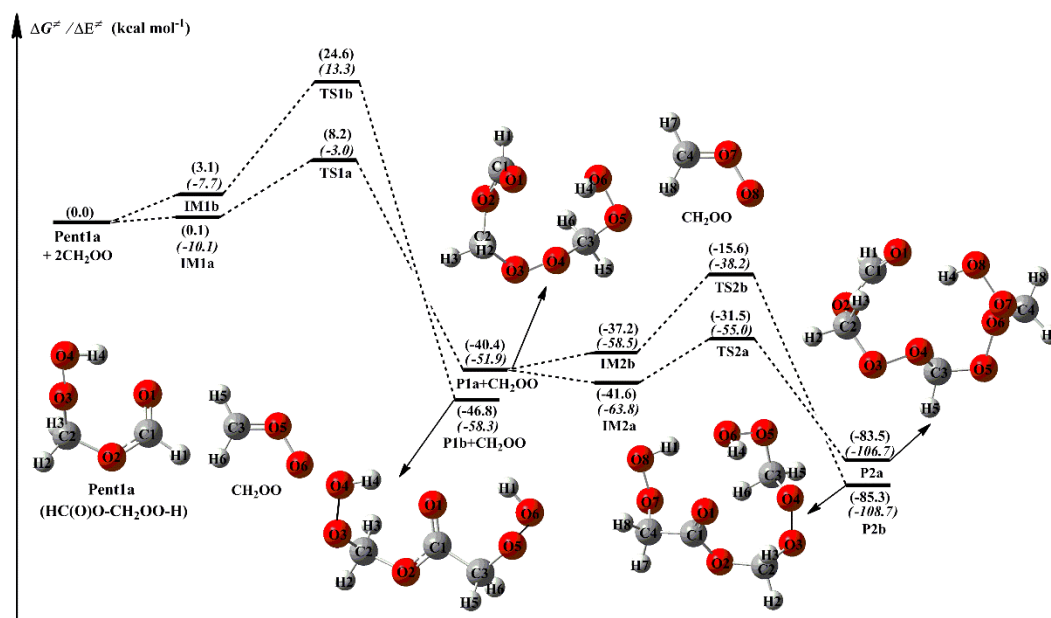
388 The simplest carbonyl oxide, CH₂OO, originates from the reaction of all terminal
389 alkenes with ozone (ozonolysis) in the atmosphere (Lin and Chao, 2017). The reaction
390 with HCOOH is expected to be one of the dominant loss processes for CH₂OO, and
391 the main product is Pent1a (also called HPMF) (Welz et al., 2014; Cabezas and Endo,
392 2019). A schematic PES for the addition reaction 2CH₂OO + Pent1a is drawn in Fig. 2,
393 and the optimized geometries of all stationary points are displayed in Fig. S3. As seen
394 in Fig. 2, the successive insertion of CH₂OO into Pent1a eventually leads to the
395 formation of oligomers P2a and P2b composed of CH₂OO as the repeat unit. These
396 oligomerization reactions are strongly exothermic and spontaneous ($> 83 \text{ kcal}\cdot\text{mol}^{-1}$),
397 implying that they are feasible thermodynamically.

398 The addition reaction 2CH₂OO + Pent1a initially proceeds through two possible
399 pathways, namely (1) –OOH insertion reaction R1a, and (2) –CH insertion reaction
400 R1b. For the –OOH insertion reaction R1a, the pre-reactive intermediate IM1a with a
401 seven-membered ring structure is formed in the entrance channel, which is stabilized
402 by the hydrogen bond interactions between the H₄ atom of Pent1a and the O₆ atom of

403 CH₂OO ($D_{(O_6-H_4)} = 1.706 \text{ \AA}$), and between the H₆ atom of CH₂OO and the O₃ atom of
404 Pent1a ($D_{(O_3-H_6)} = 2.115 \text{ \AA}$). Then IM1a converts into P1a (C₃H₆O₆, HC(O)O–
405 (CH₂OO)₂–H) via a concerted process of O₄–H₄ bond breaking in the Pent1a and
406 O₄–C₃ and H₄–O₆ bonds forming with a barrier of 8.1 kcal·mol⁻¹. For the –CH
407 insertion reaction R1b, the pre-reactive intermediate IM1b with a seven-membered
408 ring structure is formed in the entrance channel, which is stabilized by the van der
409 Waals (vdW) interactions between the O₃ atom of Pent1a and the C₃ atom of CH₂OO
410 ($D_{(O_3-C_3)} = 2.602 \text{ \AA}$), and between the O₆ atom of CH₂OO and the C₁ atom of Pent1a
411 ($D_{(O_6-C_1)} = 2.608 \text{ \AA}$). Due to the absence of hydrogen bond in IM1b, the energy of
412 IM1b is lower than that of IM1a by 3.0 kcal·mol⁻¹. IM1b transforms into P1b (C₃H₆O₆,
413 HO₂CH₂OC(O)CH₂OOH) via a concerted process of C₁–H₁ bond breaking in the
414 Pent1a and C₁–C₃ and H₁–O₆ bonds forming with a barrier of 21.5 kcal·mol⁻¹. By
415 comparing the barriers of R1a and R1b, it can be concluded that the –OOH insertion
416 reaction is favored over the –CH insertion reaction. The high reaction barrier of R1b
417 is attributed to the large bond dissociation energy (BDE) of C–H bond in the Pent1a.
418 To further insight into the reaction mechanism of R1a, the natural bond orbital (NBO)
419 analysis of the donor-accepter orbitals involved in the TS1a is performed using the
420 M06-2X wave function. The possible donor-accepter interactions are estimated by
421 using the second order perturbation theory. As illustrated in Fig. S4, the strong
422 interactions are identified as the interaction of the lone pair orbital of O₆ atom and the
423 antibonding orbital of O₄–H₄ bond, and the interaction of the lone pair orbital of O₄
424 atom and the antibonding orbital of C₃–O₅ bond.

425 Similarly, the addition reaction CH₂OO + P1a proceeds through the formation of
426 the pre-reactive intermediates IM2a and IM2b in the entrance channel, which are
427 stabilized by a hydrogen bond between the terminal oxygen atom of CH₂OO and the
428 reacting hydrogen atom of P1a, and a van der Waals (vdW) interaction between the
429 central carbon atom of CH₂OO and the carbonyl oxygen atom of P1a. The relative
430 energies of IM2a and IM2b with respect to the separate reactants P1a and CH₂OO are
431 -1.2 and 3.2 kcal·mol⁻¹, respectively, below the energies of the initial reactants
432 2CH₂OO and Pent1a are 41.6 and 37.2 kcal·mol⁻¹, respectively. Then they

433 immediately transform into the respective products P2a and P2b through the –OOH
 434 and –CH insertion transition states TS2a and TS2b with the barriers of 10.1 and 21.6
 435 kcal·mol⁻¹. This result again shows that the –OOH insertion reaction is favored
 436 kinetically. It deserves mentioning that the barrier of –OOH insertion reaction
 437 increases as the number of CH₂OO is increased. From the viewpoint of the
 438 geometrical parameters of TS2a and TS2b, the breaking O-H and C-H bonds are
 439 elongated by 14.8% and 20.6%, respectively, with respect to the equilibrium
 440 structures of IM2a and IM2b, while the forming C-O and C-C bond length are 2.013
 441 and 2.264 Å, respectively. The result reveals that TS2a and TS2b are structurally
 442 reactant-like, which are consistent with the Hammond's hypothesis that the earlier
 443 transition states are generally exothermic (Hammond, 1955).

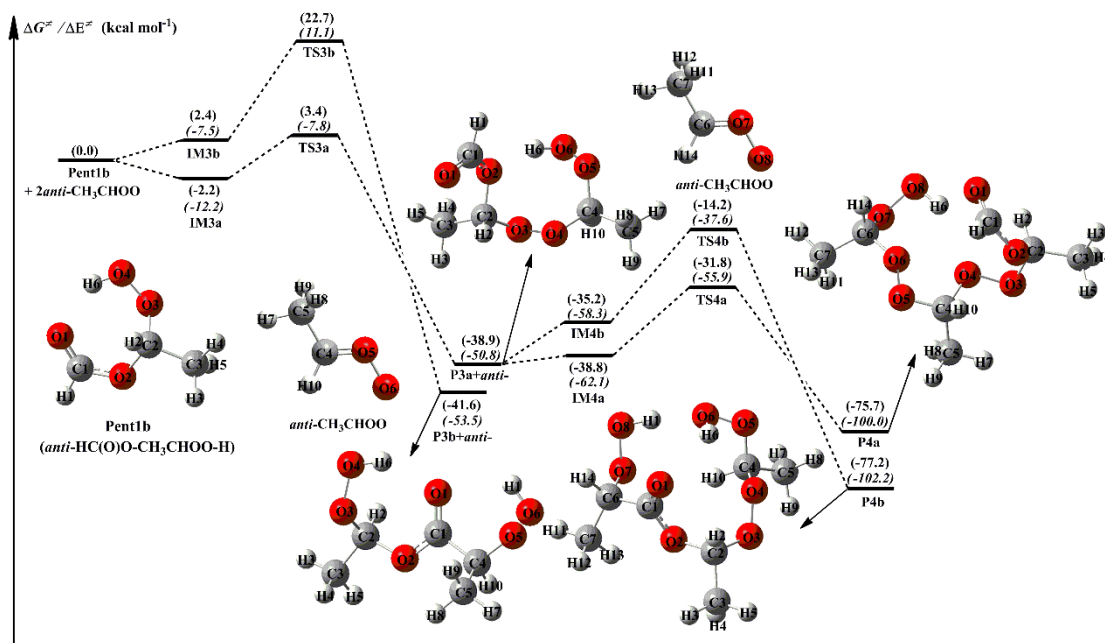


444
 445 **Figure 2.** PES (ΔG and ΔE , in italics) for the $2\text{CH}_2\text{OO} + \text{Pent1a}$ reaction at the
 446 M06-2X/ma-TZVP//M06-2X/6-311+G(2df,2p) level of theory

447 3.2.2 The reactions of *anti*-CH₃CHOO with Pent1b

448 The methyl-substituted CH₂OO has two conformers, *syn*- and *anti*-CH₃CHOO
 449 that distinguish by the orientation of methyl group relative to the terminal oxygen
 450 (Taates et al., 2013). *syn*-CH₃CHOO is more stable than *anti*-CH₃CHOO in energy
 451 due to the existence of intramolecular hydrogen bond (Long et al., 2016). The
 452 activation enthalpy of the interconversion between *syn*-CH₃CHOO and
 453 *anti*-CH₃CHOO is up to 38.5 kcal·mol⁻¹, implying that they can treat as independent

454 species in the atmosphere (Long et al., 2016; Yin and Takahashi, 2017). A schematic
455 PES for the addition reaction $2anti\text{-CH}_3\text{CHOO} + \text{Pent1b}$ is presented in Fig. 3, and
456 the optimized geometries of all stationary points are shown in Fig. S5. As shown in
457 Fig. 3, the addition reaction $2anti\text{-CH}_3\text{CHOO} + \text{Pent1b}$ proceeds through successive
458 insertion of *anti*- CH_3CHOO into Pent1b leading to the formation of oligomers P4a
459 and P4b that contain *anti*- CH_3CHOO as chain unit. The first *anti*- CH_3CHOO addition
460 reaction begins with the formation of IM3a and IM3b in the entrance channel, which
461 lie -2.2 and $2.4 \text{ kcal}\cdot\text{mol}^{-1}$ respectively, with respect to the separate reactants. Then the
462 IM3a and IM3b transform into P3a and P3b via $-\text{OOH}$ and $-\text{CH}$ insertion transition
463 states TS3a and TS3b with the barriers of 5.6 and $20.3 \text{ kcal}\cdot\text{mol}^{-1}$. This result shows
464 that the $-\text{OOH}$ insertion reaction is more favorable than the $-\text{CH}$ insertion pathway.
465 Compared with the barriers of R1a and R1b in the $2\text{CH}_2\text{OO} + \text{Pent1a}$ reaction, the
466 barriers of R3a and R3b decrease by 2.5 and $1.2 \text{ kcal}\cdot\text{mol}^{-1}$ when a methyl group is
467 introduced at the *anti*-position. The result reveals that the reactivity of
468 *anti*- CH_3CHOO is substantially higher than that of CH_2OO . This conclusion is further
469 supported by the findings of other studies, which have reported that *anti*- CH_3CHOO
470 is more reactive toward H_2O , SO_2 , and H_2O_2 than CH_2OO (Chen et al., 2017; Taatjes
471 et al., 2013; Huang et al., 2015). Similarly, the secondary *anti*- CH_3CHOO addition
472 reaction starts with the formation of IM4a and IM4b in the entrance channel with the
473 0.1 and $3.7 \text{ kcal}\cdot\text{mol}^{-1}$ stability, followed by conversion to the final products P4a and
474 P4b through the $-\text{OOH}$ and $-\text{CH}$ insertion reactions R4a and R4b. The transition
475 states TS4a and TS4b lie 7.0 and $21.0 \text{ kcal}\cdot\text{mol}^{-1}$, respectively, above the energies of
476 the respective intermediates IM4a and IM4b. This result again shows that the $-\text{OOH}$
477 insertion reaction is the most favorable channel, and the barrier increases as the
478 number of *anti*- CH_3CHOO is increased.

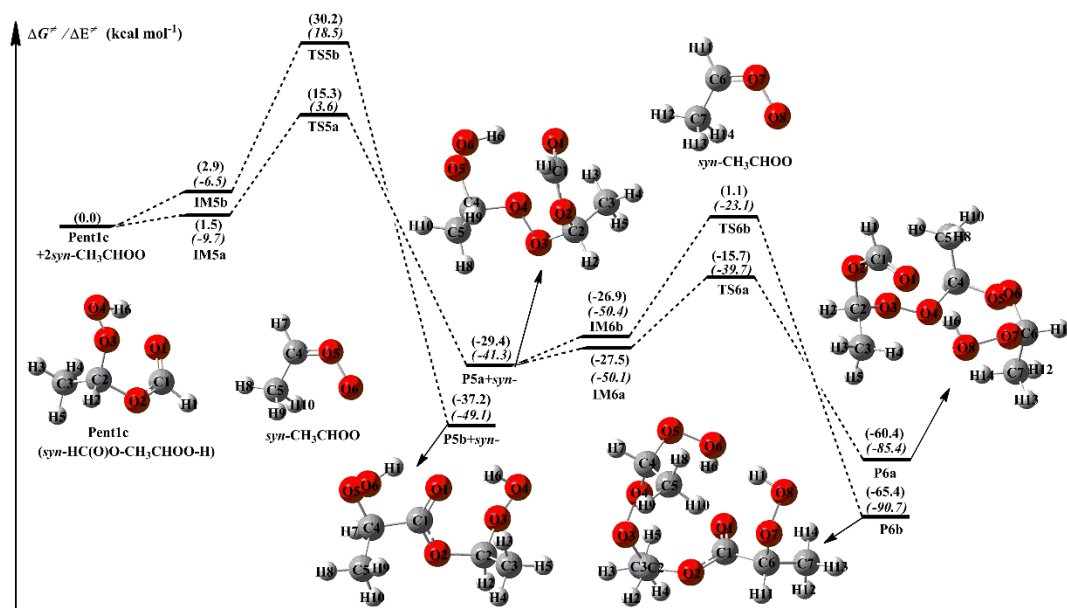


479

480 **Figure 3.** PES (ΔG and ΔE , in italics) for the $2anti\text{-CH}_3\text{CHOO} + \text{Pent1b}$ reaction at the
 481 M06-2X/ma-TZVP//M06-2X/6-311+G(2df,2p) level of theory

482 3.2.3 The reactions of *syn*-CH₃CHOO with Pent1c

483 Equivalent to the $2anti\text{-CH}_3\text{CHOO} + \text{Pent1b}$ reaction, the addition reaction
 484 $2syn\text{-CH}_3\text{CHOO} + \text{Pent1c}$ has similar transformation pathways, and is thus briefly
 485 discussed in the present study. From Fig. 4, it can be seen that the addition reaction
 486 $2syn\text{-CH}_3\text{CHOO} + \text{Pent1c}$ undergoes via successive insertion of *syn*-CH₃CHOO into
 487 Pent1c to form P6a and P6b that involve *syn*-CH₃CHOO as the repeating unit. The
 488 most favorable pathway is that the breakage of O₄-H₆ bond in the -OOH group of
 489 Pent1c occurs simultaneously with the insertion of first *syn*-CH₃CHOO into Pent1c to
 490 form P5a, followed by the insertion of secondary *syn*-CH₃CHOO into P5a to produce
 491 P6a. The barriers of these two -OOH insertion reactions R5a and R6a are 13.8 and
 492 11.8 kcal·mol⁻¹, respectively, which are higher than those of R3a and R4a in the
 493 $2anti\text{-CH}_3\text{CHOO} + \text{Pent1b}$ system by 8.2 and 4.8 kcal·mol⁻¹, respectively. The result
 494 reveals that the reactivity of *syn*-CH₃CHOO is substantially lower than that of
 495 *anti*-CH₃CHOO. Notably, the barrier of the favorable -OOH insertion pathway
 496 decreases with increasing the number of *syn*-CH₃CHOO in the $2syn\text{-CH}_3\text{CHOO} +$
 497 Pent1c reaction, which is contrary to the case of the $2\text{CH}_2\text{OO} + \text{Pent1a}$ and
 498 $2anti\text{-CH}_3\text{CHOO} + \text{Pent1b}$ reactions.



499

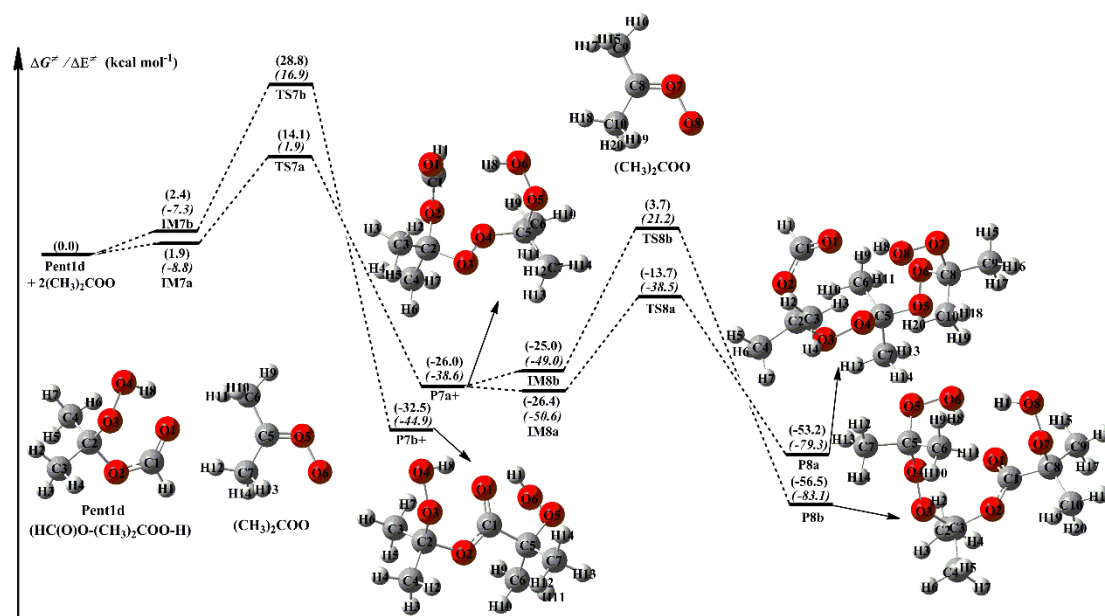
500 **Figure 4.** PES (ΔG and ΔE , in italics) for the $2\text{syn-CH}_3\text{CHOO} + \text{Pent1c}$ reaction at the
 501 M06-2X/ma-TZVP//M06-2X/6-311+G(2df,2p) level of theory

502 3.2.4 The reactions of $2(\text{CH}_3)_2\text{COO}$ with Pent1d

503 The dimethyl-substituted Criegee intermediate, $(\text{CH}_3)_2\text{COO}$, is generated from
 504 the ozonolysis of 2,3-dimethyl-2-butene in the atmosphere (Lester and Klippenstein,
 505 2018; Drozd et al., 2017; Long 2018). The bimolecular reaction of $(\text{CH}_3)_2\text{COO}$ with
 506 water is not fast enough ($k < 1.5 \times 10^{-16} \text{ cm}^3 \text{ molecule}^{-1} \text{ s}^{-1}$), while the reaction of
 507 $(\text{CH}_3)_2\text{COO}$ with HCOOH has a near gas kinetic limit rate ($k = 5.4 \times 10^{-10} \text{ cm}^3$
 508 $\text{molecule}^{-1} \text{ s}^{-1}$) (Huang et al., 2015). The result implies that a fraction of $(\text{CH}_3)_2\text{COO}$
 509 may survive under high humidity environments and react with HCOOH leading to the
 510 formation of hydroperoxide ester Pent1d. A schematic PES for the addition reaction
 511 $2(\text{CH}_3)_2\text{COO} + \text{Pent1d}$ is plotted in Fig. 5, and the optimized geometries of all
 512 stationary points are shown in Fig. S7.

513 As seen in Fig. 5, the addition reaction $2(\text{CH}_3)_2\text{COO} + \text{Pent1d}$ starts with the
 514 formation of complexes IM7a and IM7b, which lie 1.9 and 2.4 $\text{kcal}\cdot\text{mol}^{-1}$,
 515 respectively, above the energies of the separate reactants. Then they subsequently
 516 transform into products P7a and P7b through the $-\text{OOH}$ and $-\text{CH}$ insertion transition
 517 states TS7a and TS7b with the barriers of 12.2 and 26.4 $\text{kcal}\cdot\text{mol}^{-1}$. This result again
 518 shows that the $-\text{OOH}$ insertion reaction is favored over the $-\text{CH}$ insertion pathway. A
 519 similar conclusion is also obtained from the secondary $(\text{CH}_3)_2\text{COO}$ addition reaction

520 that the –OOH insertion reaction is the dominant pathway. It is of interest to compare
 521 the barriers of –OOH insertion reactions in the (CH₃)₂COO + Pent1d system with
 522 those of the analogous reactions in other SCIs + Pent1 reactions. It can be found that
 523 the barriers decrease in the order of *syn*-CH₃CHOO > (CH₃)₂COO > CH₂OO >
 524 *anti*-CH₃CHOO in the first-step SCIs addition reaction, while they become
 525 (CH₃)₂COO > *syn*-CH₃CHOO > CH₂OO > *anti*-CH₃CHOO in the second-step SCI
 526 addition pathway. The result shows that the reactivity of SCIs is significantly affected
 527 by the number and location of methyl substituents. A similar conclusion is also
 528 obtained from the thermodynamic parameters that the exothermicity of –OOH
 529 insertion reactions significantly decreases with increasing the number of methyl
 530 substituents, and the exothermicity of *anti*-methyl substituted carbonyl oxide is
 531 obviously higher than that of *syn*-methyl substituted carbonyl oxide.



532
 533 **Figure 5.** PES (ΔG and ΔE , in italics) for the $2(\text{CH}_3)_2\text{COO} + \text{Pent1d}$ reaction at the
 534 M06-2X/ma-TZVP//M06-2X/6-311+G(2df,2p) level of theory.

535 3.3 The reactions of distinct SCIs with Pent1a and implications in 536 atmospheric chemistry

537 To further elucidate the effect of the number and location of methyl substituents
 538 on the reactivity of carbonyl oxides toward hydroperoxide esters, Pent1a (also called
 539 HPMF) is selected as the model compound since it is the simplest hydroperoxide ester
 540 formed from the barrierless reaction of 1,4 O-H insertion of CH₂OO into HCOOH. As

541 mentioned above, $-OOH$ insertion reaction in the oligomerization reactions is the
542 most favorable pathway. Therefore, this type of reaction is merely considered in the
543 reactions of distinct SCIs with Pent1a. The corresponding PES and the optimized
544 geometries of all stationary points are displayed in Figs. 6 and S8, respectively. As
545 seen in Fig. 6, each pathway starts with the formation of a pre-reactive intermediate,
546 and then it overcomes a modest barrier to reaction. The barrier of the reaction of
547 CH_2OO with Pent1a is calculated to be $8.1 \text{ kcal}\cdot\text{mol}^{-1}$, which is higher than that of the
548 *anti*- $CH_3CHOO + Pent1a$ reaction by $2.5 \text{ kcal}\cdot\text{mol}^{-1}$. The reason of low barrier can be
549 explained by the NPA atomic charges, as presented in Fig. S9. As seen in Fig. S9, the
550 charges of the central carbon atom C_1 and the terminal oxygen atom O_1 of CH_2OO are
551 $0.186e$ and $-0.459e$, respectively, indicating that CH_2OO is indeed a zwitterion. The
552 C_1 atom charge becomes more positive ($0.393e$), while the O_1 atom charge becomes
553 more negative ($-0.497e$) when a methyl substituent occurs at the *anti*-position. This
554 result suggests that the *anti*-methyl substituent enhances the characteristic of carbonyl
555 oxides zwitterion and reduces the reaction barriers. Compared with the barrier of the
556 $CH_2OO + Pent1a$ reaction, the barriers increase by about $3.0 \text{ kcal}\cdot\text{mol}^{-1}$ when a
557 methyl group is introduced at the *syn*-position and dimethyl substituent. Although
558 *syn*-methyl and dimethyl substituent promote the raise of carbonyl oxides zwitterion,
559 the steric hindrance effect and intramolecular hydrogen bond are obviously dominant
560 for *syn*- CH_3CHOO and $(CH_3)_2COO$, that are not thus conducive to the nucleophilic
561 attack of hydroperoxide esters. It is worth noting that the exothermicity of distinct
562 SCIs reactions with Pent1a obviously decreases as the number of methyl group is
563 increased, and the exothermicity of *anti*-methyl substituent is higher than that of
564 *syn*-methyl substituent.

565 The rate coefficients of distinct SCIs reactions with Pent1a are calculated in the
566 temperature range of 273-400 K as summarized in Table S7. This table shows that the
567 rate coefficients k_{R1a} of the $CH_2OO + Pent1a$ reaction (R1a) decrease in the range of
568 5.0×10^{-11} (273 K) to $5.0 \times 10^{-12} \text{ cm}^3 \text{ molecule}^{-1} \text{ s}^{-1}$ (400 K) with increasing
569 temperature. A similar phenomenon is also observed from the rate coefficients of
570 Pent1a reactions with *anti*- CH_3CHOO (R9), *syn*- CH_3CHOO (R10), and $(CH_3)_2COO$

571 (R11) that they exhibit a slightly negative temperature dependence. k_{R9} is several
572 orders of magnitude greater than k_{R1a} , k_{R10} and k_{R11} in the whole temperature range,
573 suggesting that the bimolecular reaction *anti*-CH₃CHOO + Pent1a (R9) is favored
574 kinetically. Compared with the rate coefficients of R1a, the rate coefficients increase
575 by about one order of magnitude when a methyl substituent occurs at the *anti*-position,
576 whereas the rate coefficients decrease by 1 to 2 orders of magnitude when a methyl
577 group is introduced at the *syn*-position. It should be noted that although the barrier of
578 R10 is nearly identical to that of R11, k_{R10} is 1 to 2 orders of magnitude lower than
579 k_{R11} in the entire temperature range. This is probably because the rate coefficients are
580 mediated by pre-reactive intermediates that IM11 is more stable than IM10 in energy.

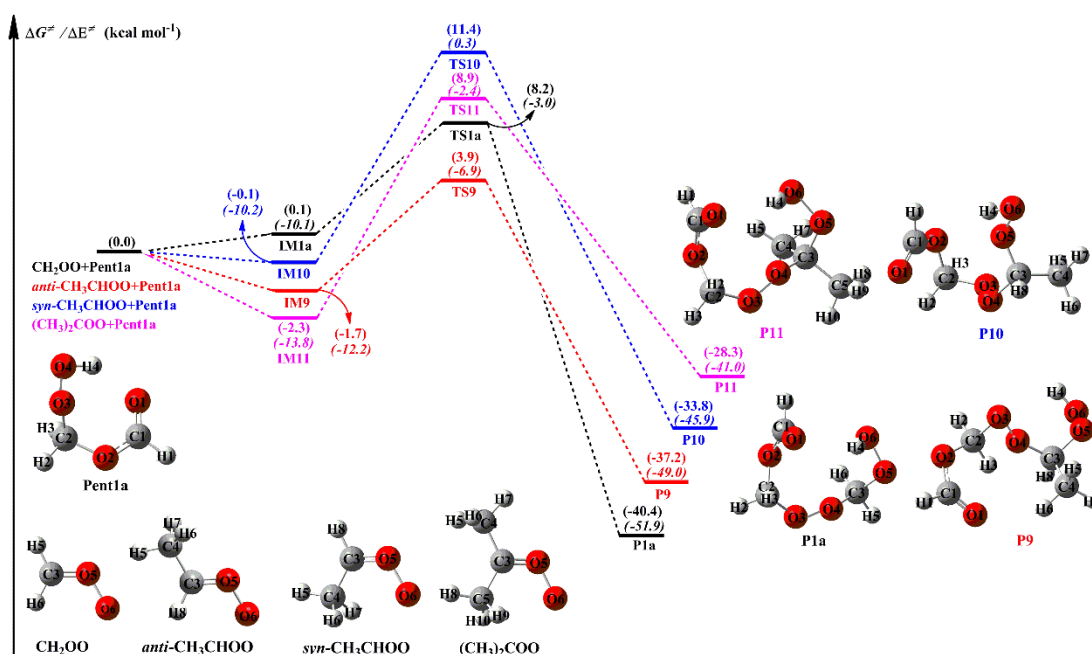
581 It is of interest to assess whether the reactions of distinct SCIs with HPMF can
582 compete well with the losses to reactions with trace species (e.g., H₂O, HCOOH and
583 SO₂), because it is well known that the reactions with trace species are expected to be
584 the dominant chemical sinks for SCIs in the atmosphere (Taatjes et al., 2013; Long et
585 al., 2016). The reported concentrations of coreactant, the rate coefficients k , and the
586 effective pseudo-first-order rate constants ($k_{\text{eff}} = k[\text{coreactant}]$) for the reactions of
587 distinct SCIs with H₂O, HCOOH, SO₂, and HPMF are summarized in Table 2. As
588 seen in Table 2, the rate coefficient of a particular SCI reaction with trace species is
589 strongly dependent on its structure. The methyl group substitution may alter the rate
590 coefficient by several to tens of times. The atmospheric concentrations of H₂O,
591 HCOOH and SO₂ in the tropical forest environments are measured to be 3.9-6.1 ×
592 10¹⁷, 5.0-10 × 10¹⁰, and 1.7-9.0 × 10¹⁰ molecules cm⁻³, respectively (Vereecken et al.,
593 2012). For the reactions of CH₂OO with H₂O, HCOOH, and SO₂, the experimental
594 rate coefficients are determined to be < 1.5 × 10⁻¹⁵, [1.1 ± 0.1] × 10⁻¹⁰, and [3.9 ± 0.7]
595 × 10⁻¹¹ cm³ molecule⁻¹ s⁻¹, respectively (Welz et al., 2012 and 2014; Chao et al., 2015),
596 which translate into $k_{\text{eff(CH}_2\text{OO+H}_2\text{O)}}$, $k_{\text{eff(CH}_2\text{OO+HCOOH)}}$ and $k_{\text{eff(CH}_2\text{OO+SO}_2)}$ of 5.9-9.2 ×
597 10², 5.5-11, and 0.7-3.5 s⁻¹, respectively. The result reveals that the reaction of
598 CH₂OO with H₂O is the most important bimolecular reaction. $k_{\text{eff(CH}_2\text{OO+HCOOH)}}$ is
599 greater by a factor of 3-8 than $k_{\text{eff(CH}_2\text{OO+SO}_2)}$, indicating that CH₂OO reaction with
600 HCOOH is favored over reaction with SO₂. Similar conclusion is also obtained from

601 the results of k_{eff} for the reactions of *anti*-CH₃CHOO, *syn*-CH₃CHOO and
602 (CH₃)₂COO with H₂O, HCOOH and SO₂ that SCIs reactions with H₂O are faster than
603 with HCOOH, which, in turn, are faster than with SO₂.

604 According to the results shown in the Table 2, the room temperature rate
605 coefficient for the reaction of CH₂OO with HPMF is calculated to be $2.7 \times 10^{-11} \text{ cm}^3$
606 $\text{molecule}^{-1} \text{ s}^{-1}$. However, to the best of our knowledge, the atmospheric concentration
607 of HPMF has not been reported up to now. We assume that the concentration of
608 HPMF is approximately equal to the atmospheric concentration of SCIs, since the
609 SCIs is the deficient reactant in the bimolecular reaction of SCIs with HCOOH.
610 Previous model-measurement studies have estimated the surface-level SCIs
611 concentrations in the range of 1.0×10^4 to $1.0 \times 10^5 \text{ molecules cm}^{-3}$ (Khan et al., 2018;
612 Novelli et al., 2017). $k_{\text{eff}(\text{CH}_2\text{OO}+\text{HPMF})}$ is calculated to be $2.7\text{-}27 \times 10^{-7} \text{ s}^{-1}$, which is
613 several orders of magnitude lower than $k_{\text{eff}(\text{CH}_2\text{OO}+\text{H}_2\text{O})}$, $k_{\text{eff}(\text{CH}_2\text{OO}+\text{HCOOH})}$ and
614 $k_{\text{eff}(\text{CH}_2\text{OO}+\text{SO}_2)}$. Similar conclusion is also obtained from the reactions of
615 *anti*-CH₃CHOO, *syn*-CH₃CHOO and (CH₃)₂COO with HPMF.

616 To further evaluate the relative importance of the complex SCIs reactions with
617 coreactant, the bimolecular reactions of methyl vinyl ketone oxide (MVK-OO) with
618 H₂O, HCOOH, SO₂, and HPMF are taken into account. MVK-OO, formed with 21 to
619 23% yield from the ozonolysis of isoprene, is a four carbon, asymmetric,
620 resonance-stabilized Criegee intermediate (Barber et al., 2018). MVK-OO has four
621 conformers, *syn-trans*-, *syn-cis*-, *anti-trans*-, and *anti-cis*- as shown in Fig. S10.
622 Herein, *syn* and *anti* refer to the orientation of the -CH₃ group relative to the terminal
623 oxygen of MVK-OO, whereas *cis* and *trans* refer to the orientation of the C₈=C₉ bond
624 relative to the C₁=O₂ bond. According to the results shown in the Fig. S10, the
625 lowest-energy conformer is *syn-trans*-MVK-OO, which is lower than *syn-cis*-,
626 *anti-trans*-, and *anti-cis*-MVK-OO by 1.42, 2.43 and 2.69 kcal·mol⁻¹, respectively.
627 Therefore, the lowest-energy conformer *syn-trans*-MVK-OO is selected as the model
628 compound to study its bimolecular reactions. As shown in Table 2, the rate coefficient
629 of H₂O reaction with *syn-trans*-MVK-OO is lower than with other SCIs by 2 to 3
630 orders of magnitude. The reason is likely to be that the existence of methyl and vinyl

631 groups hinders the occurrence of bimolecular reaction with water vapour.
 632 Consequently, a fraction of *syn-trans*-MVK-OO may survive in the presence of water
 633 vapour and react with other species. $k_{\text{eff}}(\text{MVK-OO}+\text{H}_2\text{O})$ is nearly identical to
 634 $k_{\text{eff}}(\text{MVK-OO}+\text{HCOOH})$, which is greater than $k_{\text{eff}}(\text{MVK-OO}+\text{SO}_2)$, which, in turn, is greater than
 635 $k_{\text{eff}}(\text{MVK-OO}+\text{HPMF})$ when the concentration of HPMF is equal to the atmospheric
 636 concentration of SCIs. Based on the above discussions, it can be concluded that the
 637 reactions of SCIs with HPMF is of minor importance in the atmosphere. These
 638 reactions may play a certain role in the formation and growth of organic new particle
 639 in some regions where low concentration of water vapour and high concentration of
 640 hydroperoxide esters occur.



641
 642 **Figure 6.** PES (ΔG and ΔE , in italics) for the distinct SCIs + Pent1a reactions at the
 643 M06-2X/ma-TZVP//M06-2X/6-311+G(2df,2p) level of theory

644
 645 **Table 2** The reported concentrations of coreactant, the rate coefficients k , and the effective
 646 pseudo-first-order rate constants ($k_{\text{eff}} = k[\text{coreactant}]$) for distinct SCI reactions with HPMF, H₂O,
 647 HCOOH and SO₂ at the tropical forest environments

SCIs	Coreactant	[Coreactant] (molecules cm ⁻³)	k (cm ³ molecule ⁻¹ s ⁻¹)	k_{eff} (s ⁻¹)	Reference
CH ₂ OO	H ₂ O	3.9-6.1 × 10 ¹⁷	< 1.5 × 10 ⁻¹⁵	5.9-9.2 × 10 ²	Chao et al., (2015)
	HCOOH	5.0-10.0 × 10 ¹⁰	[1.1 ± 0.1] × 10 ⁻¹⁰	5.5-11	Welz et al., (2014)

	SO ₂	1.7-9.0 × 10 ¹⁰	[3.9 ± 0.7] × 10 ⁻¹¹	0.7-3.5	Welz et al., (2012)
	HPMF	-	2.7 × 10 ⁻¹¹	-	This work
	H ₂ O	3.9-6.1 × 10 ¹⁷	[1.0 ± 0.4] × 10 ⁻¹⁴	3.9-6.1 × 10 ³	Taatjes et al., (2013)
<i>anti</i> -CH ₃ CHOO	HCOOH	5.0-10.0 × 10 ¹⁰	[5 ± 3] × 10 ⁻¹⁰	25.0-50.0	Welz et al., (2014)
	SO ₂	1.7-9.0 × 10 ¹⁰	[6.7 ± 1.0] × 10 ⁻¹¹	1.1-6.0	Taatjes et al., (2013)
	HPMF	-	3.3 × 10 ⁻¹⁰	-	This work
	H ₂ O	3.9-6.1 × 10 ¹⁷	< 4.0 × 10 ⁻¹⁵	1.6-2.4 × 10 ³	Taatjes et al., (2013)
<i>syn</i> -CH ₃ CHOO	HCOOH	5.0-10.0 × 10 ¹⁰	[2.5 ± 0.3] × 10 ⁻¹⁰	12.5-25.0	Welz et al., (2014)
	SO ₂	1.7-9.0 × 10 ¹⁰	[2.4 ± 0.3] × 10 ⁻¹¹	0.4-2.2	Taatjes et al., (2013)
	HPMF	-	1.7 × 10 ⁻¹³	-	This work
	H ₂ O	3.9-6.1 × 10 ¹⁷	< 1.5 × 10 ⁻¹⁶	58.5-91.5	Huang et al., (2015)
(CH ₃) ₂ COO	HCOOH	5.0-10.0 × 10 ¹⁰	4.5 × 10 ⁻¹⁰	22.5-45.0	Sipilä et al., (2014)
	SO ₂	1.7-9.0 × 10 ¹⁰	1.3 × 10 ⁻¹⁰	2.2-11.7	Huang et al., (2015)
	HPMF	-	2.2 × 10 ⁻¹¹	-	This work
	H ₂ O	3.9-6.1 × 10 ¹⁷	< 4.0 × 10 ⁻¹⁷	15.6-24.4	Caravan et al., (2020)
<i>syn-trans</i> -MVK	HCOOH	5.0-10.0 × 10 ¹⁰	[3.0 ± 0.1] × 10 ⁻¹⁰	15.0-30.0	Caravan et al., (2020)
-OO	SO ₂	1.7-9.0 × 10 ¹⁰	[4.2 ± 0.6] × 10 ⁻¹¹	0.7-3.8	Caravan et al., (2020)
	HPMF	-	3.0 × 10 ⁻¹¹	-	This work

648 3.4 Vapour pressure and volatility of the adduct products

649 The saturated vapour pressure (P^0) of the adduct products formed from the
650 successive reactions of SCIs with HCOOH is estimated by using the EVAPORATION
651 method proposed by Compernelle et al. (2011), and the room temperature results are

652 summarized in Table S8. This table shows that the P^0 of the adduct products decreases
653 significantly as the number of SCIs is increased. Notably, the P^0 of the adduct
654 products decreases when the size of SCIs increases. For example, the P^0 of the adduct
655 product $\text{HC(O)O(CH}_2\text{OO)}_3\text{H}$ in the $n\text{CH}_2\text{OO} + \text{HCOOH}$ reaction is estimated to be
656 3.41×10^{-5} atm, which is greater than those of the corresponding adduct products in
657 the *nanti*- $\text{CH}_3\text{CHOO} + \text{HCOOH}$ (4.73×10^{-6} atm), *nsyn*- $\text{CH}_3\text{CHOO} + \text{HCOOH}$ (4.73
658 $\times 10^{-6}$ atm), and $n(\text{CH}_3)_2\text{COO} + \text{HCOOH}$ (1.03×10^{-6} atm) reactions by 7.21, 7.21
659 and 33.11 times, respectively.

660 A classify scheme of various organic compounds is based on their volatility, as
661 presented by Donahue et al. (2012) The volatility of organic compounds is described
662 by their effective saturation concentrations. The saturated concentrations (c^0) of the
663 adduct products formed from the successive reactions of SCIs with HCOOH are listed
664 in Table S8. As shown in Table S8, the c^0 of the adduct products decrease significantly
665 as the number of SCIs is increased. It deserves mentioning that the c^0 of the adduct
666 products decrease with increasing the size of SCIs. For the $n\text{CH}_2\text{OO} + \text{HCOOH}$
667 reaction, the c^0 of the adduct products are estimated to be 1.03×10^8 ($n=1$), 5.42×10^6
668 ($n=2$), 2.53×10^5 ($n=3$), 1.11×10^4 ($n=4$) and 4.67×10^2 ($n=5$) ug/m^3 , respectively.
669 According to the Volatility Basis Set (VBS) of organic compounds (Donahue et al.,
670 2012), the adduct products belong to volatile organic compounds (VOC, $c^0 > 3 \times 10^6$
671 ug/m^3) when the number of SCIs is less than or equal to two, while they belong to
672 intermediate volatility organic compounds (IVOC, $300 < c^0 < 3 \times 10^6 \text{ ug/m}^3$) when
673 the number of SCIs is greater than or equal to three. Similarly, the adduct products in
674 the *nanti*- $\text{CH}_3\text{CHOO} + \text{HCOOH}$, *nsyn*- $\text{CH}_3\text{CHOO} + \text{HCOOH}$, and $n(\text{CH}_3)_2\text{COO} +$
675 HCOOH reactions belong to IVOC when the number of SCIs ranges from 2 to 4,
676 whereas they belong to semivolatile organic compounds (SVOC, $0.3 < c^0 < 300 \text{ ug/m}^3$)
677 when the number of SCIs is equal to 5. Based on the above discussions, it can be
678 concluded that the volatility of the adduct products is significantly affected by the
679 number and size of SCIs in the successive reaction of SCIs with HCOOH. The formed
680 adduct products may participate in the formation and growth processes of organic new
681 particle in the atmosphere.

682 4. Conclusions

683 The oligomerization reaction mechanism and kinetics of Criegee intermediates
684 reactions with their respective hydroperoxide esters as well as HPMF are investigated
685 using quantum chemical calculations and kinetics modeling methods. The main
686 conclusion is summarized as follows.

687 (a) For the initiation reactions of distinct SCIs with HCOOH, the barrierless 1,4
688 O-H insertion reaction leading to the formation of hydroperoxide esters is the most
689 favorable pathway. The exothermicity of distinct SCIs reactions with HCOOH
690 decreases when the number of methyl groups increases, and the exothermicity of the
691 *anti*-CH₃CHOO + HCOOH reaction is higher than that of the *syn*-CH₃CHOO +
692 HCOOH system.

693 (b) The addition reactions of SCIs with hydroperoxide esters proceed through
694 successive insertion of SCIs into hydroperoxide ester to form oligomers that involve
695 SCIs as the repeating unit. These oligomerization reactions are strongly exothermic
696 and spontaneous. The exothermicity of oligomerization reactions significantly
697 decreases when the number of methyl substituents increases, and the exothermicity of
698 *anti*-methyl substituted carbonyl oxides is higher than that of *syn*-methyl substituted
699 carbonyl oxides.

700 (c) The -OOH insertion reaction is favored over the -CH insertion pathway in
701 the SCIs oligomerization reactions, and the barrier heights increase with increasing
702 the number of SCIs added to the oligomer except *syn*-CH₃CHOO. The barrier of
703 -OOH insertion pathway shows a dramatic decrease when a methyl substituent occurs
704 at the *anti*-position, while it reveals a significant increase when a methyl group is
705 introduced at the *syn*-position and dimethyl substituent.

706 (d) Compared with the barrier of CH₂OO reaction with HPMF (8.1 kcal·mol⁻¹),
707 the barrier decreases by 2.5 kcal·mol⁻¹ when a methyl substituent occurs at the
708 *anti*-position, while the barrier increases by about 3.0 kcal·mol⁻¹ when a methyl group
709 is introduced at the *syn*-position and dimethyl substituent. The rate coefficients
710 increase by about one order of magnitude when a methyl substituent occurs at the

711 *anti*-position, whereas the rate coefficients decrease by 1 to 2 orders of magnitude
712 when a methyl group is introduced at the *syn*-position compared to the rate
713 coefficients of the CH₂OO + HPMF reaction.

714 (e) In the tropical forest environments, the effective pseudo-first-order rate
715 constants for the reactions of distinct SCIs with HPMF ($k_{\text{eff}}(\text{SCIs}+\text{HPMF})$) are several
716 orders of magnitude lower than those for the reactions of distinct SCIs with H₂O
717 ($k_{\text{eff}}(\text{SCIs}+\text{H}_2\text{O})$), HCOOH ($k_{\text{eff}}(\text{SCIs}+\text{HCOOH})$) and SO₂ ($k_{\text{eff}}(\text{SCIs}+\text{SO}_2)$). $k_{\text{eff}}(\text{SCIs}+\text{H}_2\text{O})$ is greater
718 than $k_{\text{eff}}(\text{SCIs}+\text{HCOOH})$, which, in turn, is greater than $k_{\text{eff}}(\text{SCIs}+\text{SO}_2)$.

719 (f) The saturated vapour pressure and saturated concentration of the adduct
720 products formed from the successive reactions of SCIs with HCOOH decrease
721 significantly as the number of SCIs is increased. The adduct products in the nCH₂OO
722 + HCOOH reactions belong to IVOC when the number of SCIs is greater than or
723 equal to 3. The adduct products in the *nanti*-CH₃CHOO + HCOOH, *nsyn*-CH₃CHOO
724 + HCOOH, and n(CH₃)₂COO + HCOOH reactions belong to IVOC when the number
725 of SCIs ranges from 2 to 4, whereas they belong to SVOC when the number of SCIs
726 is equal to 5.

727

728 **Data availability**

729 The data are accessible by contacting the corresponding author
730 (huangyu@ieecas.cn).

731

732 **Supplement**

733 The following information is provided in the Supplement: The electronic energy
734 (ΔE^\ddagger) and Gibbs free energy (ΔG^\ddagger) barriers for the initiation reactions of distinct SCIs
735 with HCOOH predicted at different levels; Enthalpies of formation for the various
736 carbonyl oxides and hydroperoxide esters; Rate coefficients of initiation reactions of
737 distinct SCIs with HCOOH; Rate coefficients of distinct SCIs reactions with HPMF;
738 Predicted saturated vapour pressure (P^0) and saturated concentrations (c^0) for the
739 adduct products; Electronic potential energy along the O-H and C-O distance

740 calculated by the M06-2X/6-311+G(2df,2p) method for the barrierless 1,4-insertion
741 reactions; Natural bond orbital (NBO) analysis of the donor-acceptor orbitals involved
742 in the TS1a; The NPA charges of different atoms in the distinct SCIs; Optimized
743 geometries of all the stationary points.

744

745 **Author contribution**

746 LC designed the study. LC and YH wrote the paper. LC performed theoretical
747 calculation. YX, ZJ, and WW analyzed the data. All authors reviewed and commented
748 on the paper.

749

750 **Competing interests**

751 The authors declare that they have no conflict of interest.

752

753 **Acknowledgments**

754 We thank Dr. Makroni Lily for valuable discussions on the barrierless 1,4 O-H
755 insertion reactions. This work was supported by the National Natural Science
756 Foundation of China (grant Nos. 42175134, 41805107, and 22002080). It was also
757 partially supported as Strategic Priority Research Program of the Chinese Academy of
758 Sciences, China (grant Nos. XDA23010300 and XDA23010000), and CAS "Light of
759 West China" Program (XAB2019B01).

760

761

762 **References**

- 763 Alecu, I. M., Zheng, J., Zhao, Y., and Truhlar, D. G.: Computational thermochemistry: scale factor
764 databases and scale factors for vibrational frequencies obtained from electronic model
765 chemistries, *J. Chem. Theory Comput.*, 6, 2872-2887, <https://doi.org/10.1021/ct100326h>,
766 2010.
- 767 Anglada, J. M., and Solé, A.: Impact of the water dimer on the atmospheric reactivity of carbonyl
768 oxides, *Phys. Chem. Chem. Phys.*, 18, 17698-17712, <https://doi.org/10.1039/C6CP02531E>,
769 2016.
- 770 Aplincourt, P., and Ruiz-López, M. F.: Theoretical study of formic acid anhydride formation from
771 carbonyl oxide in the atmosphere, *J. Phys. Chem. A*, 104, 380-388,
772 <https://doi.org/10.1021/jp9928208>, 2000.
- 773 Atkinson, R., and Arey, J.: Atmospheric degradation of volatile organic compounds, *Chem. Rev.*,
774 103, 4605-4638, <https://doi.org/10.1021/cr0206420>, 2003.
- 775 Bao, J. L., and Truhlar, D. G.: Variational transition state theory: theoretical framework and recent
776 developments, *Chem. Soc. Rev.*, 46, 7548-7596, <https://doi.org/10.1039/c7cs00602k>, 2017.
- 777 Barber, V. P., Pandit, S., Green, A. M., Trongsirawat, N., Walsh, P. J., Klippenstein, S. J., and
778 Lester, M. I.: Four-carbon Criegee intermediate from isoprene ozonolysis: methyl vinyl
779 ketone oxide synthesis, infrared spectrum, and OH production, *J. Am. Chem. Soc.*, 140,
780 10866-10880, <https://doi.org/10.1021/jacs.8b06010>, 2018.
- 781 Boys, S. F., and Bernardi, F.: The calculation of small molecular interactions by the differences of
782 separate total energies. Some procedures with reduced errors, *Mol. Phys.*, 19, 553-566,
783 <https://doi.org/10.1080/00268977000101561>, 1970.
- 784 Cabezas, C., and Endo, Y.: Observation of hydroperoxyethyl formate from the reaction between
785 the methyl Criegee intermediate and formic acid, *Phys. Chem. Chem. Phys.*, 22, 446-454,
786 <https://doi.org/10.1039/C9CP05030B>, 2020.
- 787 Cabezas, C., and Endo, Y.: The Criegee intermediate-formic acid reaction explored by rotational
788 spectroscopy, *Phys. Chem. Chem. Phys.*, 21, 18059-18064,
789 <https://doi.org/10.1039/c9cp03001h>, 2019.
- 790 Cabezas, C., and Endo, Y.: The reactivity of the Criegee intermediate CH₃CHOO with water
791 probed by FTMW spectroscopy, *J. Chem. Phys.*, 148, 014308-014315,
792 <https://doi.org/10.1063/1.5009033>, 2018.
- 793 Canneaux, S., Bohr, F., and Henon, E.: KiSThEP: a program to predict thermodynamic properties
794 and rate constants from quantum chemistry results, *J. Comput. Chem.*, 35, 82-93,
795 <https://doi.org/10.1002/jcc.23470>, 2013.
- 796 Caravan, R. L., Vansco, M. F., Au, K., Khan, M. A. H., Li, Y. L., Winiberg, F. A. F., Zuraski, K.,
797 Lin, Y. H., Chao, W., Trongsirawat, N., Walsh, P. J., Osborn, D. L., Percival, C. J., Lin, J. J.
798 M., Shallcross, D. E., Sheps, L., Klippenstein, S. J., Taatjes, C. A., and Lester, M. I.: Direct
799 kinetic measurements and theoretical predictions of an isoprene-derived Criegee intermediate,
800 *Proc. Natl. Acad. Sci. U.S.A.*, 117, 9733-9740, <https://doi.org/10.1073/pnas.1916711117>,
801 2020.
- 802 Chaliyakunnel, S., Millet, D. B., Wells, K. C., Cady-Pereira, K. E., and Shephard, M. W.: A large
803 underestimate of formic acid from tropical fires: constraints from space-borne measurements,
804 *Environ. Sci. Technol.*, 50, 5631-5640, <https://doi.org/10.1021/acs.est.5b06385>, 2016.

805 Chao, W., Hsieh, J. T., Chang, C. H., and Lin, J. J. M.: Direct kinetic measurement of the reaction
806 of the simplest Criegee intermediate with water vapor, *Science*, 347, 751-754,
807 <https://doi.org/10.1126/science.1261549>, 2015.

808 Chen, L., Huang, Y., Xue, Y., Cao J., and Wang, W.: Effect of oligomerization reactions of Criegee
809 intermediate with organic acid/peroxy radical on secondary organic aerosol formation from
810 isoprene ozonolysis, *Atmos. Environ.*, 187, 218-229,
811 <https://doi.org/10.1016/j.atmosenv.2018.06.001>, 2018.

812 Chen, L., Huang, Y., Xue, Y., Cao, J., and Wang, W.: Competition between HO₂ and H₂O₂
813 reactions with CH₂OO/*anti*-CH₃CHOO in the oligomer formation: a theoretical perspective, *J.*
814 *Phys. Chem. A*, 121, 6981-6991, <https://doi.org/10.1021/acs.jpca.7b05951>, 2017.

815 Chen, L., Huang, Y., Xue, Y., Shen, Z., Cao, J., and Wang, W.: Mechanistic and kinetics
816 investigations of oligomer formation from Criegee intermediate reactions with hydroxyalkyl
817 hydroperoxides, *Atmos. Chem. Phys.*, 19, 4075-4091,
818 <https://doi.org/10.5194/acp-19-4075-2019>, 2019.

819 Chen, L., Wang, W., Wang, W., Liu, Y., Liu, F., Liu, N., and Wang, B: Water-catalyzed
820 decomposition of the simplest Criegee intermediate CH₂OO, *Theor. Chem. Acc.*, 135,
821 131-143, <https://doi.org/10.1007/s00214-016-1894-9>, 2016.

822 Chhantyal-Pun, R., McGillen, M. R., Beames, J. M., Khan, M. A. H., Percival, C. J., Shallcross, D.
823 E., and Orr-Ewing, A. J.: Temperature Dependence of the Rates of Reaction of Trifluoroacetic
824 Acid with Criegee Intermediates, *Angew. Chem. Int. Ed.*, 129, 9172-9175,
825 <https://doi.org/10.1002/anie.201703700>, 2017.

826 Chhantyal-Pun, R., Rotavera, B., McGillen, M. R., Khan, M. A. H., Eskola, A. J., Caravan, R. L.,
827 Blacker, L., Tew, D. P., Osborn, D. L., Percival, C. J., Taatjes, C. A., Shallcross D. E., and
828 Orr-Ewing, A. J.: Criegee intermediate reactions with carboxylic acids: a potential source of
829 secondary organic aerosol in the atmosphere, *ACS Earth Space Chem.*, 2, 833-842,
830 <https://doi.org/10.1021/acsearthspacechem.8b00069>, 2018.

831 Chung, C. A., Su, J. W., and Lee, Y. P.: Detailed mechanism and kinetics of the reaction of Criegee
832 intermediate CH₂OO with HCOOH investigated via infrared identification of conformers of
833 hydroperoxymethyl formate and formic acid anhydride, *Phys. Chem. Chem. Phys.*, 21,
834 21445-21455, <https://doi.org/10.1039/c9cp04168k>, 2019.

835 Compernelle, S., Ceulemans, K., and Müller, J. F.: EVAPORATION: a new vapour pressure
836 estimation method for organic molecules including non-additivity and intramolecular
837 interactions, *Atmos. Chem. Phys.*, 11, 9431-9450, <https://doi.org/10.5194/acp-11-9431-2011>,
838 2011.

839 Criegee, R.: Mechanism of ozonolysis, *Angew. Chem. Int. Ed. Engl.*, 14, 745-752,
840 <https://doi.org/10.1002/anie.197507451>, 1975.

841 Donahue, N. M., Kroll, J. H., Pandis, S. N., and Robinson, A. L.: A two-dimensional volatility
842 basis set – Part 2: Diagnostics of organic-aerosol evolution, *Atmos. Chem. Phys.*, 12,
843 615-634, <https://doi.org/10.5194/acp-12-615-2012>, 2012.

844 Drozd, G. T., Kurtén, T., Donahue, N. M., and Lester, M. I.: Unimolecular decay of the
845 dimethyl-substituted Criegee intermediate in alkene ozonolysis: decay time scales and the
846 importance of tunneling, *J. Phys. Chem. A*, 121, 6036-6045,
847 <https://doi.org/10.1021/acs.jpca.7b05495>, 2017.

848 Eckart, C.: The penetration of a potential barrier by electrons, *Phys. Rev.*, 35, 1303-1309,

849 <https://doi.org/10.1103/PhysRev.35.1303>, 1930.

850 Frisch, M. J., Trucks, G. W., Schlegel, H. B., Scuseria, G. E., Robb, M. A., Cheeseman, J. R.,
851 Montgomery, J. A. Jr., Vreven, T., Kudin, K. N., Burant, J. C., Millam, J. M., Iyengar, S. S.,
852 Tomasi, J., Barone, V., Mennucci, B., Cossi, M., Scalmani, G., Rega, N., Petersson, G. A.,
853 Nakatsuji, H., Hada, M., Ehara, M., Toyota, K., Fukuda, R., Hasegawa, J., Ishida, M.,
854 Nakajima, T., Honda, Y., Kitao, O., Nakai, H., Klene, M., Li, X., Knox, J. E., Hratchian, H. P.,
855 Cross, J. B., Adamo, C., Jaramillo, J., Gomperts, R., Stratmann, R. E., Yazyev, O., Austin, A.
856 J., Cammi, R., Pomelli, C., Ochterski, J. W., Ayala, P. Y., Morokuma, K., Voth, G. A.,
857 Salvador, P., Dannenberg, J. J., Zakrzewski, V. G., Dapprich, S., Daniels, A. D., Strain, M. C.,
858 Farkas, O., Malick, D. K., Rabuck, A. D., Raghavachari, K., Foresman, J. B., Ortiz, J. V., Cui,
859 Q., Baboul, A. G., Clifford, S., Cioslowski, J., Stefanov, B. B., Liu, G., Liashenko, A.,
860 Piskorz, P., Komaromi, I., Martin, R. L., Fox, D. J., Keith, T., Al-Laham, M. A., Peng, C. Y.,
861 Nanayakkara, A., Challacombe, M., Gill, P. M. W., Johnson, B., Chen, W., Wong, M. W.,
862 Gonzalez, C., and Pople, J. A.: Gaussian 09, Revision D.01; Gaussian, Inc.: Wallingford, CT,
863 2009.

864 Fukui, K.: The path of chemical reactions - the IRC approach, *Acc. Chem. Res.*, 14, 363-368,
865 <https://doi.org/10.1021/ar00072a001>, 1981.

866 Giorio, C., Campbell, S. J., Bruschi, M., Tampieri, F., Barbon, A., Toffoletti, A., Tapparo, A.,
867 Paijens, C., Wedlake, A. J., Grice, P., Howe, D. J., and Kalbere, M.: Online quantification of
868 Criegee intermediates of α -pinene ozonolysis by stabilization with spin traps and
869 proton-transfer reaction mass spectrometry detection, *J. Am. Chem. Soc.*, 139, 3999-4008,
870 <https://doi.org/10.1021/jacs.6b10981>, 2017.

871 Gong, Y., and Chen, Z.: Quantification of the role of stabilized Criegee intermediates in the
872 formation of aerosols in limonene ozonolysis, *Atmos. Chem. Phys.*, 21, 813-829,
873 <https://doi.org/10.5194/acp-21-813-2021>, 2021.

874 Hammond, G. S.: A correlation of reaction rates, *J. Am. Chem. Soc.*, 77, 334-338,
875 <https://doi.org/10.1021/ja01607a027>, 1955.

876 Huang, H. L., Chao, W., and Lin, J. J. M.: Kinetics of a Criegee intermediate that would survive
877 high humidity and may oxidize atmospheric SO₂, *Proc. Natl. Acad. Sci. U.S.A.*, 112,
878 10857-10862, <https://doi.org/10.1073/pnas.1513149112>, 2015.

879 Humphrey, W., Dalke, A., and Schulten, K.: VMD: Visual molecular dynamics, *J. Molec.*
880 *Graphics*, 14, 33-38, [https://doi.org/10.1016/0263-7855\(96\)00018-5](https://doi.org/10.1016/0263-7855(96)00018-5), 1996.

881 Johnson, D., and Marston, G.: The gas-phase ozonolysis of unsaturated volatile organic
882 compounds in the troposphere, *Chem. Soc. Rev.*, 37, 699-716,
883 <https://doi.org/10.1039/B704260B>, 2008.

884 Johnson, D., Lewin, A. G., and Marston, G.: The effect of Criegee-intermediate scavengers on the
885 OH yield from the reaction of ozone with 2-methylbut-2-ene, *J. Phys. Chem. A*, 105,
886 2933-2935, <https://doi.org/10.1021/jp003975e>, 2001.

887 Karton, A., Kettner, M., and Wild, D. A.: Sneaking up on the Criegee intermediate from below:
888 Predicted photoelectron spectrum of the CH₂OO⁻ anion and W3-F12 electron affinity of
889 CH₂OO, *Chem. Phys. Lett.*, 585, 15-20, <https://doi.org/10.1016/j.cplett.2013.08.075>, 2013.

890 Khan, M. A. H., Percival, C. J., Caravan, R. L., Taatjes, C. A., and Shallcross, D. E.: Criegee
891 intermediates and their impacts on the troposphere, *Environ. Sci.: Processes Impacts*, 20,
892 437-453, <https://doi.org/10.1039/C7EM00585G>, 2018.

893 Lester, M. I., and Klippenstein, S. J.: Unimolecular decay of Criegee intermediates to OH radical
894 products: prompt and thermal decay processes, *Acc. Chem. Res.*, 51, 978-985,
895 <https://doi.org/10.1021/acs.accounts.8b00077>, 2018.

896 Lin, J. J. M., and Chao, W.: Structure-dependent reactivity of Criegee intermediates studied with
897 spectroscopic methods, *Chem. Soc. Rev.*, 46, 7483-7497, <https://doi.org/10.1039/c7cs00336f>,
898 2017.

899 Lin, X., Meng, Q., Feng, B., Zhai, Y., Li, Y., Yu, Y., Li, Z., Shan, X., Liu, F., Zhang, L., and Sheng,
900 L.: Theoretical study on Criegee intermediate's role in ozonolysis of acrylic acid, *J. Phys.*
901 *Chem. A*, 123, 1929-1936, <https://doi.org/10.1021/acs.jpca.8b11671>, 2019.

902 Liu, F., Beames, J. M., Petit, A. S., McCoy, A. B., and Lester, M. I.: Infrared-driven unimolecular
903 reaction of CH₃CHOO Criegee intermediates to OH radical products, *Science*, 345,
904 1596-1598, <https://doi.org/10.1126/science.1257158>, 2014.

905 Liu, L., Bei, N., Wu, J., Liu, S., Zhou, J., Li, X., Yang, Q., Feng, T., Cao, J., Tie, X., and Li, G.:
906 Effects of stabilized Criegee intermediates (sCIs) on sulfate formation: a sensitivity analysis
907 during summertime in Beijing-Tianjin-Hebei (BTH), China, *Atmos. Chem. Phys.*, 19,
908 13341-13354, <https://doi.org/10.5194/acp-19-13341-2019>, 2019.

909 Long, B., Bao, J. L., and Truhlar, D. G.: Atmospheric chemistry of Criegee intermediates:
910 unimolecular reactions and reactions with water, *J. Am. Chem. Soc.*, 138, 14409-14422,
911 <https://doi.org/10.1021/jacs.6b08655>, 2016.

912 Long, B., Bao, J. L., and Truhlar, D. G.: Unimolecular reaction of acetone oxide and its reaction
913 with water in the atmosphere, *Proc. Natl. Acad. Sci. U.S.A.*, 115, 6135-6140,
914 <https://doi.org/10.1073/pnas.1804453115>, 2018.

915 Long, B., Cheng, J. R., Tan, X. F., and Zhang, W. J.: Theoretical study on the detailed reaction
916 mechanisms of carbonyl oxide with formic acid, *J. Mol. Struct.: Theochem*, 916, 159-167,
917 <https://doi.org/10.1016/j.theochem.2009.09.028>, 2009.

918 Lu, T., and Chen, F.: Multiwfn: A multifunctional wavefunction analyzer, *J. Comput. Chem.*, 33,
919 580-592, <https://doi.org/10.1002/jcc.22885>, 2012.

920 Mendes, J., Zhou, C. W., and Curran, H. J.: Theoretical chemical kinetic study of the H-atom
921 abstraction reactions from aldehydes and acids by H atoms and OH, HO₂, and CH₃ radicals, *J.*
922 *Phys. Chem. A*, 118, 12089-12104, <https://doi.org/10.1021/jp5072814>, 2014.

923 Neeb, P., Horie, O., and Moortgat, G. K.: The ethene-ozone reaction in the gas phase, *J. Phys.*
924 *Chem. A*, 102, 6778-6785, <https://doi.org/10.1021/jp981264z>, 1998.

925 Novelli, A., Hens, K., Ernest, C. T., Martinez, M., Nölscher, A. C., Sinha, V., Paasonen, P., Petäjä,
926 T., Sipilä, M., Elste, T., Plass-Dülmer, C., Phillips, G. J., Kubistin, D., Williams, J.,
927 Vereecken, L., Lelieveld, J., and Harder, H.: Estimating the atmospheric concentration of
928 Criegee intermediates and their possible interference in a FAGE-LIF instrument, *Atmos.*
929 *Chem. Phys.*, 17, 7807-7826, <https://doi.org/10.5194/acp-17-7807-2017>, 2017.

930 Novelli, A., Vereecken, L., Lelieveld, J., and Harder, H.: Direct observation of OH formation from
931 stabilised Criegee intermediates, *Phys. Chem. Chem. Phys.*, 16, 19941-19951,
932 <https://doi.org/10.1039/c4cp02719a>, 2014.

933 Osborn, D. L., and Taatjes, C. A.: The physical chemistry of Criegee intermediates in the gas
934 phase, *Int. Rev. Phys. Chem.*, 34, 309-360, <https://doi.org/10.1080/0144235X.2015.1055676>,
935 2015.

936 Paulot, F., Wunch, D., Crouse, J. D., Toon, G. C., Millet, D. B., DeCarlo, P. F., Vigouroux, C.,

937 Deutscher, N. M., Abad, G. G., Notholt, J., Warneke, T., Hannigan, J. W., Warneke, C., de
938 Gouw, J. A., Dunlea, E. J., Mazière, M. D., Griffith, D. W. T., Bernath, P., Jimenez, J. L., and
939 Wennberg, P. O.: Importance of secondary sources in the atmospheric budgets of formic and
940 acetic acids, *Atmos. Chem. Phys.*, 11, 1989-2013, <https://doi.org/10.5194/acp-11-1989-2011>,
941 2011.

942 Peltola, J., Seal, P., Inkilä, A., and Eskola, A.: Time-resolved, broadband UV-absorption
943 spectrometry measurements of Criegee intermediate kinetics using a new photolytic
944 precursor: unimolecular decomposition of CH₂OO and its reaction with formic acid, *Phys.*
945 *Chem. Chem. Phys.*, 22, 11797-11808, <https://doi.org/10.1039/d0cp00302f>, 2020.

946 Porterfield, J. P., Lee, K. L. K., Dell'Isola, V., Carroll, P. B., and McCarthy, M. C.:
947 Characterization of the simplest hydroperoxide ester, hydroperoxymethyl formate, a
948 precursor of atmospheric aerosols, *Phys. Chem. Chem. Phys.*, 21, 18065-18070,
949 <https://doi.org/10.1039/c9cp03466h>, 2019.

950 Riva, M., Budisulistiorini, S. H., Zhang, Z., Gold, A., Thornton, J. A., Turpin, B. J., and Surratt, J.
951 D.: Multiphase reactivity of gaseous hydroperoxide oligomers produced from isoprene
952 ozonolysis in the presence of acidified aerosols, *Atmos. Environ.*, 152, 314-322,
953 <https://doi.org/10.1016/j.atmosenv.2016.12.040>, 2017.

954 Sadezky, A., Winterhalter, R., Kanawati, B., Rompp, A., Spengler, B., Mellouki, A., Bras, G. L.,
955 Chaimbault, P., and Moortgat, G. K.: Oligomer formation during gas-phase ozonolysis of
956 small alkenes and enol ethers: new evidence for the central role of the Criegee Intermediate
957 as oligomer chain unit, *Atmos. Chem. Phys.*, 8, 2667-2699,
958 <https://doi.org/10.5194/acp-8-2667-2008>, 2008.

959 Sakamoto, Y., Inomata, S., and Hirokawa, J.: Oligomerization reaction of the Criegee intermediate
960 leads to secondary organic aerosol formation in ethylene ozonolysis, *J. Phys. Chem. A*, 117,
961 12912-12921, <https://doi.org/10.1021/jp408672m>, 2013.

962 Sakamoto, Y., Yajima, R., Inomata, S., and Hirokawa, J.: Water vapour effects on secondary
963 organic aerosol formation in isoprene ozonolysis, *Phys. Chem. Chem. Phys.*, 19, 3165-3175,
964 <https://doi.org/10.1039/c6cp04521a>, 2017.

965 Sipilä, M., Jokinen, T., Berndt, T., Richters, S., Makkonen, R., Donahue, N. M., Mauldin III, R. L.,
966 Kurtén, T., Paasonen, P., Sarnela, N., Ehn, M., Junninen, H., Rissanen, M. P., Thornton, J.,
967 Stratmann, F., Herrmann, H., Worsnop, D. R., Kulmala, M., Kerminen, V. M., and Petäjä, T.:
968 Reactivity of stabilized Criegee intermediates (sCIs) from isoprene and monoterpene
969 ozonolysis toward SO₂ and organic acids, *Atmos. Chem. Phys.*, 14, 12143-12153,
970 <https://doi.org/10.5194/acp-14-12143-2014>, 2014.

971 So, S., Wille, U., and Silva, G. D.: Atmospheric chemistry of enols: a theoretical study of the vinyl
972 alcohol + OH + O₂ reaction mechanism, *Environ. Sci. Technol.*, 48, 6694-6701,
973 <https://doi.org/10.1021/es500319q>, 2014.

974 Stavrakou, T., Müller, J. F., Peeters, J., Razavi, A., Clarisse, L., Clerbaux, C., Coheur, P. F.,
975 Hurtmans, D., Mazière, M. D., Vigouroux, C., Deutscher, N. M., Griffith, D. W. T., Jones, N.,
976 and Paton-Walsh, C.: Satellite evidence for a large source of formic acid from boreal and
977 tropical forests, *Nat. Geosci.*, 5, 26-30, <https://doi.org/10.1038/ngeo1354>, 2012.

978 Taatjes, C. A., Khan, M. A. H., Eskola, A. J., Percival, C. J., Osborn, D. L., Wallington, T. J., and
979 Shallcross, D. E.: Reaction of perfluorooctanoic acid with Criegee intermediates and
980 implications for the atmospheric fate of perfluorocarboxylic acids, *Environ. Sci. Technol.*, 53,

981 1245-1251, <https://doi.org/10.1021/acs.est.8b05073>, 2019.

982 Taatjes, C. A., Welz, O., Eskola, A. J., Savee, J. D., Scheer, A. M., Shallcross, D. E., Rotavera, B.,
983 Lee, E. P. F., Dyke, J. M., Mok, D. K. W., Osborn, D. L., and Percival, C. J.: Direct
984 measurements of conformer-dependent reactivity of the Criegee intermediate CH_3CHOO ,
985 *Science*, 340, 177-180, <https://doi.org/10.1126/science.1234689>, 2013.

986 Taatjes, C. A.: Criegee intermediates: what direct production and detection can teach us about
987 reactions of carbonyl oxides, *Annu. Rev. Phys. Chem.*, 68, 183-207,
988 <https://doi.org/10.1146/annurev-physchem-052516-050739>, 2017.

989 Tobias, H. J., and Ziemann, P. J.: Kinetics of the gas-phase reactions of alcohols, aldehydes,
990 carboxylic acids, and water with the C^{13} stabilized Criegee intermediate formed from
991 ozonolysis of 1-tetradecene, *J. Phys. Chem. A*, 105, 6129-6135,
992 <https://doi.org/10.1021/jp004631r>, 2001.

993 Truhlar, D. G., Hase, W. L., and Hynes, J. T.: Current status of transition-state theory, *J. Phys.*
994 *Chem.*, 87, 2664-2682, <https://doi.org/10.1021/jp953748q>, 1996.

995 Vansco, M. F., Zuraski, K., Winiberg, F. A. F., Au, K., Trongsiwat, N., Walsh, P. J., Osborn, D. L.,
996 Percival, C. J., Klippenstein, S. J., Taatjes, C. A., Lester, M. I., and Caravan, R. L.:
997 Functionalized hydroperoxide formation from the reaction of methacrolein-oxide, an
998 isoprene-derived Criegee intermediate, with formic acid: experiment and theory, *Molecules*,
999 26, 3058-3072, <https://doi.org/10.3390/molecules26103058>, 2021.

1000 Vereecken, L., Harder, H., and Novelli, A.: The reaction of Criegee intermediates with NO , RO_2 ,
1001 and SO_2 , and their fate in the atmosphere, *Phys. Chem. Chem. Phys.*, 14, 14682-14695,
1002 <https://doi.org/10.1039/c2cp42300f>, 2012.

1003 Vereecken, L.: The reaction of Criegee intermediates with acids and enols, *Phys. Chem. Chem.*
1004 *Phys.*, 19, 28630-28640, <https://doi.org/10.1039/c7cp05132h>, 2017.

1005 Wang, S., Newland, M. J., Deng, W., Rickard, A. R., Hamilton, J. F., Muñoz, A., Ródenas, M.,
1006 Vázquez, M. M., Wang, L., and Wang, X.: Aromatic photo-oxidation, a new source of
1007 atmospheric acidity, *Environ. Sci. Technol.*, 54, 7798-7806,
1008 <https://doi.org/10.1021/acs.est.0c00526>, 2020.

1009 Welz, O., Eskola, A. J., Sheps, L., Rotavera, B., Savee, J. D., Scheer, A. M., Osborn, D. L., Lowe,
1010 D., Booth, A. M., Xiao, P., Khan, M. A. H., Percival, C. J., Shallcross, D. E., and Taatjes, C.
1011 A.: Rate coefficients of C(1) and C(2) Criegee intermediate reactions with formic and acetic
1012 Acid near the collision limit: direct kinetics measurements and atmospheric implications,
1013 *Angew. Chem. Int. Ed.*, 53, 4547-4550, <https://doi.org/10.1002/anie.201400964>, 2014.

1014 Welz, O., Savee, J. D., Osborn, D. L., Vasu, S. S., Percival, C. J., Shallcross, D. E., and Taatjes, C.
1015 A.: Direct kinetic measurements of Criegee intermediate (CH_2OO) formed by reaction of
1016 CH_2I with O_2 , *Science*, 335, 204-207, <https://doi.org/10.1126/science.1213229>, 2012.

1017 Yin, C., and Takahashi, K.: How does substitution affect the unimolecular reaction rates of
1018 Criegee intermediates? *Phys. Chem. Chem. Phys.*, 19, 12075-12084,
1019 <https://doi.org/10.1039/c7cp01091e>, 2017.

1020 Yu, S.: Role of organic acids (formic, acetic, pyruvic and oxalic) in the formation of cloud
1021 condensation nuclei (CCN): a review, *Atmos. Res.*, 53, 185-217,
1022 [https://doi.org/10.1016/S0169-8095\(00\)00037-5](https://doi.org/10.1016/S0169-8095(00)00037-5), 2000.

1023 Zhang, P., Wang, W., Zhang, T., Chen, L., Du, Y., Li, C., and Lv, J.: Theoretical study on the
1024 mechanism and kinetics for the self-reaction of $\text{C}_2\text{H}_5\text{O}_2$ radicals, *J. Phys. Chem. A*, 116,

1025 4610-4620, <https://doi.org/10.1021/jp301308u>, 2012.

1026 Zhao, R., Kenseth, C. M., Huang, Y., Dalleska, N. F., Kuang, X. M., Chen, J., Paulson, S. E., and
1027 Seinfeld, J. H.: Rapid aqueous-phase hydrolysis of ester hydroperoxides arising from Criegee
1028 intermediates and organic acids, *J. Phys. Chem. A*, 122, 5190-5201,
1029 <https://doi.org/10.1021/acs.jpca.8b02195>, 2018.

1030 Zhao, Y., and Truhlar, D. G.: The M06 suite of density functionals for main group
1031 thermochemistry, thermochemical kinetics, noncovalent interactions, excited states, and
1032 transition elements: two new functionals and systematic testing of four M06-class functionals
1033 and 12 other functionals, *Theor. Chem. Acc.*, 120, 215-241,
1034 <https://doi.org/10.1007/s00214-007-0310-x>, 2008.

1035 Zhao, Y., Wingen, L. M., Perraud, V., Greaves, J., and Finlayson-Pitts, B. J.: Role of the reaction
1036 of stabilized Criegee intermediates with peroxy radicals in particle formation and growth in
1037 air, *Phys. Chem. Chem. Phys.*, 17, 12500-12514, <https://doi.org/10.1039/c5cp01171j>, 2015.

1038 Zheng, J., Bao, L. J., Meana-Paneda, R., Zhang, S., Lynch, B. J., Corchado, J. C., Chuang, Y. Y.,
1039 Fast, P. L., Hu, W. P., Liu, Y. P., Lynch, G. C., Nguyen, K. A., Jackels, C. F.,
1040 Fernandez-Ramos, A., Ellingson, B. A., Melissas, V. S., Villa, J., Rossi, I., Coitino, L., Pu, J.,
1041 Albu, T. V., Steckler, R., Garrett, B. C., Issacson, A. D., and Truhlar, D. G.: Polyrate, version
1042 2017-C, University of Minnesota: Minneapolis, MN, 2018.

1043 Zhou, S., Joudan, S., Forbes, M. W., Zhou, Z., and Abbatt, J. P. D.: Reaction of condensed-phase
1044 Criegee intermediates with carboxylic acids and perfluoroalkyl carboxylic acids, *Environ. Sci.
1045 Technol. Lett.*, 6, 243-250, <https://doi.org/10.1021/acs.estlett.9b00165>, 2019.